Department of Physics and
Astronomy
University of Heidelberg

In partial fulfillment of the requirements
for the degree of
MASTER OF SCIENCE

submitted by

Lennart Aufleger
born in Aurich (Germany)

2016

Measurement of electron dynamics in atoms and molecules with intense XUV FEL radiation

This master's thesis has been conducted by
Lennart Aufleger
at the
Max-Planck-Institut für Kernphysik
under the supervision of
Prof. Thomas Pfeifer

Abstract

Measurement of electron dynamics in atoms and molecules with intense XUV FEL radiation

The observation of strong-field dynamics in atoms and molecules on ultra short timescales has been of high interest for a long time. In recent years the investigation of inner-shell electron dynamics became possible when strong ultrashort lasers in the extreme ultra violet (XUV) became reality in the form of free electron lasers (FEL). They allow for example the observation of charge transfer processes in molecules.
In this spirit a measurement campaign was performed at FLASH (DESY), to investigate such phenomena at halogenated hydrocarbon molecules. This thesis describes the required further development of a transient absorption beam line and the new design of essential components with regards to experiments with corrosive targets and an FEL light source.
An intensity dependent absorption measurement of a doubly excited state in helium was conducted as well. This can be considered an extension of prior work performed recently with near infrared and visible (VIS) strong-field modification of XUV absorption from lab-based HHG light source. The measurement described in this work investigates XUV strong-field modification of XUV absorption with partially coherent FEL light.

Zusammenfassung

Messung von Elektronendynamik in Atomen und Molekülen mit intensiver XUV FEL-Strahlung

Seit langer Zeit ist die Beobachtung von Dynamiken in Atomen und Molekülen auf ultrakurzen Zeitskalen von großem Interesse. In den letzten Jahren ist die Untersuchung der Elektronendynamik auf den inneren Schalen möglich geworden, da starke ultrakurze Laser mit extrem ultravioletten (XUV) Spectrum in Form von Freien-Elektronen-Lasern Realität wurden. Diese ermöglichen zum Beispiel die Beobachtung von Ladungsaustausch-Prozessen in Molekülen.
In diesem Kontext wurde eine Messkampagne am FLASH (DESY) durchgeführt, um solche Phänomene an halogenierten Kohlenwasserstoffen zu untersu-

chen. Diese Arbeit beschreibt die dafür notwendige Weiterentwicklung eines Transienten-Absorptions-Experiments und das Neudesignen von essentiellen Bestandteile im Hinblick auf Experimente mit korrosiven Substanzen und einer FEL Strahlungsquelle.
Zusätzlich wurde eine intensitätsabhängige Absorptionsmessung an doppelt angeregtem Helium durchgeführt. Dies steht in einer Linie mit kürzlich durchgeführten Messungen, die Starkfeld-Modifikationen von XUV Absorptionslinien durch nah-infrarotes und sichtbares Licht einer HHG-Quelle zeigen. Die Messungen im Rahmen dieser Arbeit behandeln die Starkfeld-Modifikationen dieser Absorptionslinie unter Anwendung partiell kohärenten XUV Lichts eines FELs.

Contents

Introduction

When Ugo Fano 1961 presented a full description of auto ionizing states [1], it marked a starting point for a variety of investigations into electron-electron interaction. This based on the general concept of his work, which can be understood as the interference of two quantum paths. When two electrons are simultaneously excited (double excitation), this discrete bound state is embedded in the continuum above the ionization threshold. It decays by relaxing one electron back to its ground state, while ionizing the other one (auto ionization). The relative phase and therefore the interference of the two pathways (direct photo ionization and auto ionization) gives insight into electron electron correlation. This information can be extracted from the absorption line shape of the transition.
First investigations were realized soon after Fano's work was published. Due to the lack strong field coherent light sources in the extreme ultra violet (XUV) spectral region, the observation of the interaction of doubly excited states and Fano resonances was not yet possible.
This was circumvented recently by additional coupling of a strong field in the visible (VIS) spectral region, which led to changes in the absorption line shape induced by the pondoromotive potential [2]. This implies not only the measurement but the direct manipulation of such state.
With the opportunity for experiments with a high intense XUV light source, the next step was the investigation of strong-field modification directly with XUV on the absorption line in the same spectral region. The experiment and results are presented in Ch.3

Another field of interest is the electron dynamic in molecules. To investigate for example the charge transfer, strongly localized core-level electrons in the constituents are probed. Halogenated hydro carbons represent a good playground for such experiments, since the halogen atoms on both sides can be

manipulated and probed in a site selective manner (resonant core excitations with the XUV) while the charge is delocalized over the carbon chain. A sufficient yield in the spectroscopic signal in combination with the core level excitation demands for an intense light source in the XUV spectral region.
In order to carry out such an experiment, significant changes were introduced to a novel transient absorption beam line as a part of this work. A detailed description of the concepts and the implementation is presented in Ch. 2.

The first chapter provides an introduction to the theoretical background of Fano's theory, strong field effects and the concept of free electron lasers (FEL), which represented the high intense (partially) coherent XUV light source to the experiments performed.

1 Theoretical Background

The experiment treated in this thesis is an intensity dependent measurement of helium in an transient absorption spectroscopy setup. In this context the theoretical background of linear absorption is described in Ch. 1.1. Since the intensities reach up to 10^{14} W/cm^2, strong field effects have to be considered, in Ch.1.2.
The atomic state under investigation is the auto ionizing doubly excited state. It exhibits a asymmetric line shape due to the configuration interaction of the electrons. This was firstly described be Ugo Fano [1]. A short excerpt of this theory will be presented in Ch. 1.3. Extensions to his theory have been conducted for the strong field regime by Lambropoulos and Zoller and will be treated in Ch. 1.3.2. Also the extension to time-dependent dipole perspective is of interest since it allows the mapping of the asymmetry parameter q to the phase shift of a state.
Helium is the most simple atomic system providing two electrons. It is therefore the object of investigation and is treated in Ch. 1.4
Finally some light will be shed on the light source utilized in this work. The theoretical concept of a free electron laser (FEL) by the means of the Free electron LAser Hamburg (FLASH) will be explained in Ch. 1.5.

1.1 Linear absorption

As light propagates through matter, interactions with the constituents occur. Besides other processes discussed later, the light-matter interaction can lead to absorption of photons. The attenuation of the light can be described by Lambert-Beer´s law

$$I(\omega, z) = I_0(\omega, z) \cdot exp[-\rho_N \cdot \sigma(\omega) \cdot z] \tag{1.1}$$

where σ describes the cross section of the process, ρ_N the number density of the medium and z the interaction length. This law is limited to dilute targets though, where it can be assumed that each photon interacts only once. For higher densities propagation effects have to be considered. Equation (1.1) describes the attenuated intensity $I(\omega, z)$ after the light of an original intensity $I_0(\omega)$ has propagated a distance z in the medium. For a fixed density the macroscopic quantity absorption is presented by the coefficient $\alpha(\omega)$. It is connected to the microscopic quantity cross section $\sigma(\omega)$ via the atomic number density

$$\alpha(\omega) = \rho_N \cdot \sigma(\omega) \tag{1.2}$$

To determine this quantity, one has to take a look at the process of absorption. An electromagnetic field induces a dipole on the microscopic level with the moment

$$\boldsymbol{\mu} = -e \cdot \mathbf{r}. \tag{1.3}$$

On the macroscopic level this results in the polarization of the ensemble

$$P(\omega) = \rho_N \cdot \langle \mu(\omega) \rangle \tag{1.4}$$

which is proportional to the expectation value of the microscopic dipole $\mu(\omega)$ and the atomic number density ρ_N.

The polarization is also connected to the electric field amplitude via the dielectric susceptibility

$$\mathbf{P}(\omega) = \varepsilon_0 \cdot \left(\sum_i \bar{\chi}^{(i)} \cdot \mathbf{E}^i \right). \tag{1.5}$$

Since the experiments in this thesis were performed with dilute targets in the gas phase, which are by default isotropic, the tensor and vector description can be disregarded. For simplicity high order terms are neglected here as well. The effect of nonlinear polarization on absorption and coherence effects are further described in [3] [4]. The complex dielectric susceptibility $\chi(\omega) = \chi'(\omega) + i \cdot \chi''(\omega)$

is connected to the refractive index via

$$n(\omega) = \sqrt{1+\chi(\omega)} \approx 1 + \frac{\chi'(\omega)}{2} + i \cdot \frac{\chi''(\omega)}{2} \tag{1.6}$$

where the approximation is valid for very small susceptibilities only. For cases where the approximation does not hold, dispersion and absorption cannot be disentangled which would require a full calculation of Maxwell's equations for the propagation. The wave vector is then given as

$$k(\omega) = \frac{\omega}{c} \cdot n = \frac{\omega}{c} \cdot \left(1 + \frac{\chi'(\omega)}{2} + i \cdot \frac{\chi''(\omega)}{2}\right). \tag{1.7}$$

Inserting this into the complex wave function $E(x,\omega) = E_0 \exp[ik(\omega) \cdot x]$ and comparing it by $I(x,\omega) = E(x,\omega)^2$ to the absorption law above, the imaginary part is linearly linked to the absorption coefficient $\alpha(\omega) = \omega/c \cdot \chi''(\omega)$. Therefore the microscopic cross section can be written as

$$\sigma(\omega) \propto \frac{\omega}{c}\frac{1}{\rho_N}\mathrm{Im}(\chi) = \frac{\omega}{c}\frac{1}{\rho_N}\,\mathrm{Im}\left(\frac{\mu(\omega)}{E(\omega)}\right). \tag{1.8}$$

In order to actually derive this cross section, one has to calculate the susceptibility for the bound state of interest.
For this purpose, consider a two level system with groundstate $|g\rangle$ and excited state $|\varphi\rangle$. It is excited by a resonant photon at $t = 0$. In the perturbation limit, the system is then in a coherent superposition of both states. As both states differ in their eigenenergies, their phases evolve differently, leading to an oscillating dipole moment. Also, both states are still eigenstates of the system, hence could live infinitely. However the electromagnetic coupling to vacuum fluctuations induces an exponential decay of this superposition state with the lifetime $1/\Gamma$. The time evolution of the coefficient c_φ for $t \geq 0$ is then given by

$$c_\varphi(t) = -\frac{i}{\hbar}\,\mu_{\varphi,0} \cdot e^{-i\frac{E_\varphi}{\hbar}\,t}\; e^{-\frac{\Gamma}{2}\,t} \tag{1.9}$$

with $\mu_{\varphi,0} = \langle \varphi \,|\, \hat{\mu} \,|\, g \rangle$ the dipole transition matrix element. The spectrum of the transition is then determined by the Fourier transformation of the coefficient

$$\tilde{c}_\varphi(E) = i\,\frac{\mu_{\varphi,0}}{\frac{\Gamma\hbar}{2} - i\,(E - E_\varphi)}. \tag{1.10}$$

This leads to the dielectric susceptibility

$$\chi(E) \propto i \frac{|\mu_{\varphi,0}|^2}{\frac{\Gamma\hbar}{2} - i\,(E - E_\varphi)} \propto -\frac{E - E\varphi}{(\frac{\Gamma\hbar}{2})^2 + (E - E_\varphi)^2} + i \frac{\frac{\Gamma\hbar}{2}}{(\frac{\Gamma\hbar}{2})^2 + (E - E_\varphi)^2}. \tag{1.11}$$

From Eq. (1.8) the imaginary term can be identified as proportional to the absorption. The real term corresponds to the dispersion of the system. The corresponding line shapes for both are depicted in Fig. 1.1.

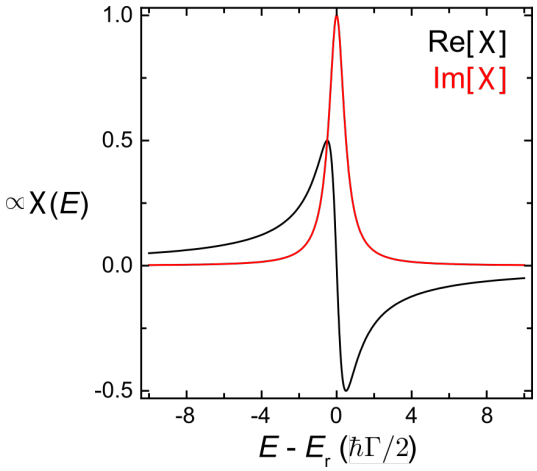

Figure 1.1: Real part (black) and imaginary part (red) of the dielectric susceptibility for a exponentially decaying (Lorentzian) bound state. Reprinted from [5]

In absorption spectroscopy, the optical density OD, also known as absorbance, is the observable commonly used as the basis for physical interpretations. It is defined by the negative logarithm of the ratio of the measured and the incoming spectral intensity. The latter is measured as reference before the target.

$$OD = -log_{10}\left(\frac{I(\omega)}{I_0(\omega)}\right) = \frac{\sigma(\omega)}{\ln 10} \cdot \rho_N \cdot z. \tag{1.12}$$

1.2 Strongfield regime

Intensities on the order of 10^{16} W/cm^2 can be achieved at FLASH. These intensities cannot be treated perturbatively since the field strength is on the order of the inner atomic forces. New effects like the transfer of population between the states, known as Rabi oscillation, as well as the splitting and

the shift of energy levels, known as AC-Stark or Autler-Townes splitting, can occur. Since these effects can be explained with only two states, an interaction of such system ($|\phi_m\rangle$, $|\phi_n\rangle$) with a monochromatic laser shall be considered. The frequency of its field (ω_c) is close to the transition frequency of the states ($\omega_{nm} \approx \omega_c$). The Hamiltonian of the system can be expressed as

$$\hat{\mathbf{H}} = \hat{\mathbf{H}}_0 + \hat{\boldsymbol{\mu}} \cdot E(t) \tag{1.13}$$

where the Hamiltonian $\hat{\mathbf{H}}_0$ yields the energy of the eigenstates of the field free system while the dipole operator $\hat{\boldsymbol{\mu}}$ enables the coupling and hence the transition between both states. The new system can be written as a superposition of both states

$$|\Psi(t)\rangle = c_n(t)\ |\phi_n\rangle + c_m(t)\ |\phi_m\rangle\,. \tag{1.14}$$

Solving the Schrödinger equation for this system

$$i\hbar \frac{d}{dt} |\Psi(t)\rangle = \hat{\mathbf{H}} |\Psi(t)\rangle\,, \tag{1.15}$$

a set of coupled linear differential equation emerges which have to be solved for the time-dependent coefficients $c_n(t), c_m(t)$.

$$i\hbar \frac{d}{dt} \begin{pmatrix} c_n(t) \\ c_m(t) \end{pmatrix} = \mathbf{H} \cdot \begin{pmatrix} c_n(t) \\ c_m(t) \end{pmatrix} \tag{1.16}$$

The coupling matrix

$$\mathbf{H} = \begin{pmatrix} E_n & \mu_{nm}\, E(t) \\ \mu^*_{nm}\, E(t) & E_m \end{pmatrix} \tag{1.17}$$

contains the eigenenergies E_n and E_m of the field-free Hamiltonian $\hat{\mathbf{H}}_0$ as diagonal elements. The dipole matrix elements μ_{nm} of the dipole operator contributes only off-diagonal elements, representing the coupling of the states. This description is without loss of generality and can be extended to any finite number of states. Hence these equations qualify for numerical treatments. Analytical solutions with certain approximations are possible for specific cases. They give physical insight into effects as discussed in the following.

The approximation utilized here is the rotating-wave approximation. For this purpose, the coefficients are rotated in phase

$$c_{n,m}(t) = \tilde{c}_{n,m}(t) \cdot \exp[-i(\omega_{n,m} \mp \Delta/2)\, t] \tag{1.18}$$

with the detuning $\Delta = (\omega_n - \omega_m) - \omega_c$ of the laser frequency from the energy spacing of the two levels. The real electric field $E(t) = E_0 \cos(\omega_c t)$ is expanded into a complex function and the rotating wave approximation applied thereafter. The treatment disregards terms with rapid oscillating phases of frequency $(\omega_n - \omega_m) + \omega_c$. In this rotating frame the coupled linear differential equations change their appearance and the new coupling matrix is given by

$$\mathbf{H}^{rot} = \begin{pmatrix} \Delta & \Omega_R \\ \Omega_R^* & -\Delta \end{pmatrix} \tag{1.19}$$

with $\Omega_R = \mu_{nm} E_0/\hbar$ the Rabi frequency. The eigenvalues are determined as

$$\lambda_{1,2} = \pm\frac{\hbar}{2}\sqrt{\Delta^2 + |\Omega_R|^2}. \tag{1.20}$$

Since these are the eigenvalues of the new system, they are time-independent. Converting back into the non-rotating frame, they are centered at both eigenengeries of the field free system.

$$\begin{aligned} E_n^{\pm} &= E_n - \frac{\hbar\Delta}{2} \pm \frac{\hbar}{2}\sqrt{\Delta^2 + |\Omega_R|^2} \\ E_m^{\pm} &= E_m + \frac{\hbar\Delta}{2} \pm \frac{\hbar}{2}\sqrt{\Delta^2 + |\Omega_R|^2} \end{aligned} \tag{1.21}$$

The new eigenstates resulting from the presence of a detuned monochromatic intense laser are called dressed states. Two consequences can be derived from Eq. (1.21). The dressing induces a splitting of the field-free levels. It is proportional to the detuning ($\hbar\Delta$). These dressed states are constant for low field intensities or weak coupling. For rising field intensities or increasing coupling, these levels start to repel each other further and the impact of the detuning can be neglected. The splitting of the energy levels is then proportional to the Rabi frequency ($\hbar|\Omega_R|$). This effect is is called AC Stark splitting and is illustrated in Fig. 1.2

If now a weak laser is used to probe these levels from a third level, the

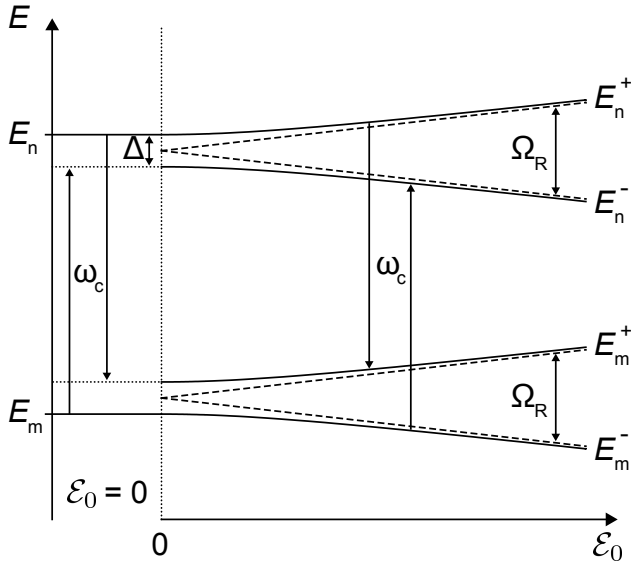

Figure 1.2: Illustration of the AC Stark effect. The two levels $|n\rangle$ $|m\rangle$ are coupled by a strong laser field $E_0 \cos(\omega_c t)$, leading to the splitting of the energy levels and the repulsion with increasing intensity, corresponding to Eqs. (1.21). Reprinted from [6]

observed absorption lines are known as the Autler-Townes doublet. With the diagonalized Hamiltonian, which delivered the eigenenergies in (1.21), the new coefficients can be determined as well. Since the new states of the dressed system are eigenstates they are stationary. With them the dynamics of the time-depend coefficients $\tilde{c}_{n,m}(t)$ can be evaluated:

$$\begin{aligned} \tilde{c}_n(t) &= -i\frac{\Omega_R}{\Omega'_R}\sin\frac{\Omega'_R}{2}\cdot t \\ \tilde{c}_n(t) &= \cos\frac{\Omega'_R}{2}\cdot t + i\frac{\Delta}{\Omega'_R}\sin\frac{\Omega'_R}{2}\cdot t \end{aligned} \tag{1.22}$$

These equations (1.22) allow the interpretation of the Rabi frequency in the first place. The population $|c_{n,m}|^2$ of the states oscillates back and forth between them with the Rabi frequency Ω_R or more precisely with the generalized Rabi frequency $\Omega'_R = \sqrt{|\Omega_r|^2 + \Delta^2}$ in the case of non-zero detuning. The initial condition to Eq. (1.22) is that the entire population is in the lower state ($|\tilde{c}_n(0)|^2 = 0$, $|\tilde{c}_m(0)|^2 = 1$). Hence the Rabi frequency presents a characteristic entity for the dynamic of the dressed system.
When the Rabi cycle is on the order of the lifetime of a state, further effects can be found. In an intuitive picture, a state with short lifetime $|s\rangle$ is coupled to a

state with long lifetime $|l\rangle$. When the coupling and field strength are chosen such that a Rabi-cycle is on the order of the lifetime of $|s\rangle$, the population is transferred to the longer living state before $|s\rangle$ can decay. This changes the effective lifetime of $|s\rangle$ and in turn impacts the absorption line shape of the state. Hence also continuous lasers can influence dynamical systems.
So far the amplitude of the dressing electromagnetic field was assumed constant. For pulses with a slowly varying envelope the Rabi frequency still corresponds to $\Omega_R = \mu_{n,m} E_0(t)/\hbar$. Although, when the envelope varies rapidly on the order of a Rabi cycle, the interpretation of the time-dependent Raby frequency may loose its validity and a numerical approach may be necessary. Further effects have to be considered and will be discussed in detail for autoionizing states in Ch.1.3.2.

1.3 Auto-ionizing states

An auto-ionizing state describes a configuration where two electrons are excited simultaneously. The energy of such states is high enough to directly ionize a single electron, but since it is split between two electrons it is still a bound state. Hence the state is energetically embedded in the continuum and therefore degenerate. After a certain lifetime the state decays non-radiatively by relaxing one electron to the ground state while emitting the other one, known as the Auger decay. A typical lifetime, e.g. of the helium 2s2p state is 17fs. The line shape of such a state exhibits an asymmetry in opposite to the Lorentzian, which would correspond to an exponential decay as described in Ch. 1.1. It was first observed by H. Beutler in 1935. The asymmetric appearance can be explained by the fact that both channels, the direct ionization and the auto ionization, provide the same final state and exhibit the same energy [1]. Hence they can be considered interfering quantum paths, yielding this line shape and providing the concept of a quantum interferometer. It has been utilized successfully to investigate e.g. electron-electron correlation [2].

1.3.1 Fano's original work

In the 1960s Ugo Fano presented a formalism to describe the auto-ionizing state and its line shape [1]. It is based on the interaction of the doubly excited state

with the continuum states. It is a general concept and can be applied whenever two channels are present, leading to the same final state and interfering with each other, especially when involving discrete and continuum states. The original work of Fano was time-independent and completely in the energy domain. Rabi-cycling and strong-field laser interaction in a time dependent model were developed later and are discussed subsequently. In his original work Fano describes the interaction of both states as configuration interaction. Due to the interaction, both states are no longer eigenstates but can be used as the elements of a full basis set for new eigenstates. In absence of external fields the Hamiltonian $\hat{\mathbf{H}}$ with its elements

$$\begin{aligned} \left\langle \varphi \left| \hat{\mathbf{H}} \right| \varphi \right\rangle &= E_{\varphi} \\ \left\langle \chi_{E'} \left| \hat{\mathbf{H}} \right| \varphi \right\rangle &= V_{E'} \\ \left\langle \chi_{E'} \left| \hat{\mathbf{H}} \right| \chi_{E''} \right\rangle &= E' \, \delta(E'' - E') \end{aligned} \tag{1.23}$$

is diagonalized. The ground state is disregarded as it can be assumed energetically far away from the doubly excited states. It will be accounted for later by the transition $\hat{\mathbf{T}}$ to the configuration states. The eigenvalues on the diagonal of the coupling matrix, E and E' describe the former eigenenergies of the interaction-free system. The interaction of the discrete double-exited state $|\varphi\rangle$ with the continuum states $|\chi\rangle_E$ are introduced by $V_{E'}$. The eigenstates of the diagonalized Hamiltonian can be expressed as

$$|\Psi_E\rangle = a_E \, |\varphi\rangle + \int dE' \, b_{EE'} \, |\chi_{E'}\rangle \, . \tag{1.24}$$

where the energy-dependent expansion coefficients a_E and $b_{EE'}$ have to be determined as the next step. Two conditions for the energy expectation value and normalization of the new eigenstates

$$\left\langle \Psi_E \left| \hat{\mathbf{H}} \right| \Psi_E \right\rangle = E \tag{1.25}$$

$$\langle \Psi_E \, | \, \Psi_{\bar{E}} \rangle = \delta(E - \bar{E}) \tag{1.26}$$

yield two equations for two unknown coefficients. In combination with the equations above, the coefficients result to

$$a_E = \frac{\sin \Delta_E}{\pi V_E} \tag{1.27}$$

$$b_{EE'} = \frac{V_{E'}}{\pi V_E} \frac{\sin \Delta_E}{E - E'} - \delta(E - E') \cos \Delta_E \tag{1.28}$$

with Δ_E given as

$$\Delta_E = -\arctan \frac{\pi |V_E|^2}{E - E_\varphi - F(E)} \tag{1.29}$$

with the energy shift

$$F(E) = \mathscr{P} \int dE' \frac{|V_E|^2}{E - E_\varphi}. \tag{1.30}$$

The eigenstates can be expressed as

$$|\Psi_E\rangle = \frac{\sin \Delta_E}{\pi V_E} |\Phi\rangle + \cos \Delta_E |\chi_E\rangle \tag{1.31}$$

with the modified bound state

$$|\Phi\rangle = |\varphi\rangle + \mathscr{P} \int dE' \frac{V_E}{E - E'} |\chi\rangle_{E'} . \tag{1.32}$$

Here as well as in Eq. (1.30), the operator $\mathscr{P}$ presents the principle value of the integral. This serves to circumvent the pole at $E = E'$ with integration in the complex plane, which was used by Fano in his original work in form of scattering theory. The modification in the second term in (1.32) implies a direct mix of the original bound state $|\varphi\rangle$ with the continuum states $|\chi_{E'}\rangle$ due to the configuration interaction $V_{E'}$.
The dimensionless argument of (1.29) can be condensed to the reduced energy

$$\varepsilon = \frac{E - (E_\varphi + F(E))}{\Gamma/2} = \frac{E - E_\Phi}{\Gamma/2} \tag{1.33}$$

with

$$\Gamma = 2\pi |V_E|^2 \tag{1.34}$$

Slight changes in ε on the scale of Γ result in a rapid change in the new eigenstate expansion (1.31) centered at $E = E_\Phi$. The parameters can therefore be identified as the resonance energy E_Φ and the line width Γ corresponding to the lifetime h/Γ of this auto-ionizing state.
The symmetries of the trigonometric functions in (1.31) result in constructive and destructive interference of the two configuration states $|\Phi\rangle$ and $|\chi_{E'}\rangle$ on either side of the resonance energy, resulting in an asymmetric line shape. This can be parametrized by the q parameter

$$q = \frac{\left\langle \Phi \middle| \hat{\mathbf{T}} \middle| g \right\rangle}{\pi V_E^* \left\langle \chi_E \middle| \hat{\mathbf{T}} \middle| g \right\rangle}. \tag{1.35}$$

To deduce the origin of this parameter, consider the expectation value of the transition $\hat{\mathbf{T}}$ from an initial state, e.g. the groundstate $|g\rangle$, into the double-exited state Ψ_E with respect to the quantum mechanical channel of the transition into the continuum $\left\langle \chi_{E'} \middle| \hat{\mathbf{T}} \middle| g \right\rangle$. This can be parametrizied as

$$\frac{|\left\langle \Psi_E \middle| \hat{\mathbf{T}} \middle| g \right\rangle|^2}{|\left\langle \chi_E \middle| \hat{\mathbf{T}} \middle| g \right\rangle|^2} = \frac{|q+\varepsilon|^2}{1+\varepsilon^2}. \tag{1.36}$$

Line shapes for different values of q are depicted in Fig. 1.3

The experimentally obtained spectra are fitted with

$$\sigma = a \cdot \frac{|q+\varepsilon|^2}{1+\varepsilon^2} + \sigma_{NR} \tag{1.37}$$

with the parameter a being the relative strength to the non-resonant cross section σ_{NR}.

1.3.2 extension of Fano's theory

Autoionizing states in strong fields To account for higher intensities, which are expected to play are role in this work, the perturbative approach can no longer be utilized as in the previous chapter. For strong fields, effects like Rabi-cycling and state dressing can occur, as discussed in Ch. 1.2. A time-dependent model becomes necessary. This extension to Fano's theory was performed by Lambropoulos and Zoller [7]. They presented an analytical

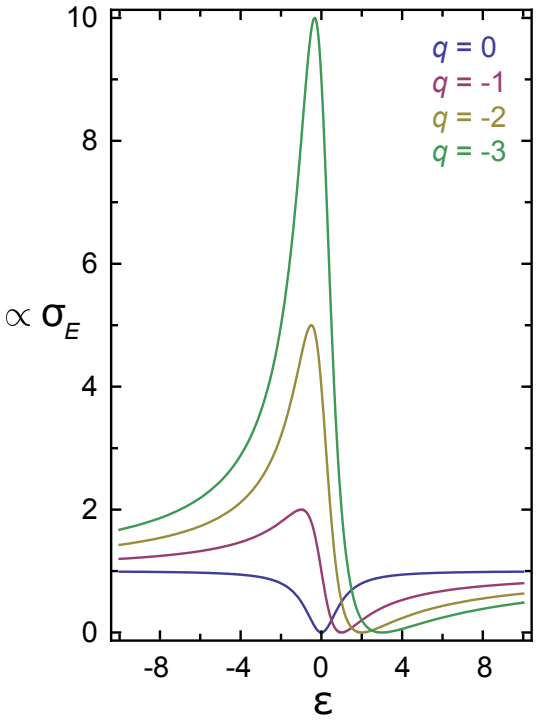

Figure 1.3: Fano line shape of Eq. (1.36) for different asymmetry parameters as a function of the reduced energy ε. Reprinted from [6]

framework which could describe the interaction of auto-ionizing states in strong laser fields.

The starting point is the utilization of the already diagonalized state $|\Psi_E\rangle$ Eq. (1.31) of the perturbativ case. This state is coupled non-perturbatively to the ground state $|g\rangle$. The system then can be expressed as a superposition

$$|\tilde{\Psi}(t)\rangle = c_g(t)\ |g\rangle + \int dE'\, c_{E'}\ |\Psi_{E'}\rangle\,. \tag{1.38}$$

The Schrödinger-equation has to be solved for the full Hamiltonian containing the coupling by the field

$$\hat{\mathbf{H}} = \hat{\mathbf{H}}_0 + \hat{\boldsymbol{\mu}} \cdot E(t). \tag{1.39}$$

As both states in (1.38) are eigenstates of $\hat{\mathbf{H}}_0$ but not of the coupled system, the time evolution of $c_g(t)$ and $c_{E'}(t)$ originating from the coupling $\hat{\boldsymbol{\mu}}E$ has to be determined. The electromagnetic field is assumed monochromatic and the rotating-wave approximation is applied. The mathematical description is much more sophisticated at this point since the auto-ionizing states are not discrete

but a structured continuum (Eq. (1.38)). The result contains, among other things, the identification of the effective Rabi-frequency. For further details be referred to [7].

A time-dependent perspective on the Fano phase: The original theory developed by Fano established a connection between the asymmetry of the line shape and the q-parameter. Hence the resonance line shape can be characterized by the resonance energy E_Ψ, the line width Γ and the the q-parameter.
The linear dipole response of an atomic system can then be described by

$$\tilde{d}(t) \propto c_q \delta(t) + \exp\Big[\underbrace{-\frac{\Gamma}{2}t}_{(a)} + i\Big(\underbrace{-\frac{E_\Psi}{\hbar}t}_{(b)} + \underbrace{\varphi(q)}_{(c)}\Big)\Big]. \tag{1.40}$$

The term for the exponential decay (a) and the phase evolution (b) of a Lorentzian can be identified. However, the phase evolution is shifted (c) by a q-parameter-depending offset $\varphi(q)$. The mapping of the offset phase to the q-parameter was developed in recent years [2],[8]:

$$\begin{aligned} \varphi(q) &= 2 \cdot \arg(q - i) \\ q(\varphi) &= -\cot\Big(\frac{\varphi}{2}\Big). \end{aligned} \tag{1.41}$$

It is illustrated in Fig. 1.4. This phase shift and in turn the change in the q-parameter can be introduced by several effects. The fundamental reason is the configuration interaction discussed above, Ch. 1.3.1. Furthermore the shift can be induced by manipulating the states. This can happen either perturbatively via the ponderomotive potential $U_P = \frac{e^2 E_0^2}{4m\omega^2}$ or by dressing via an intense laser field as discussed in Ch. 1.2. The dipole response for these cases is also illustrated in Fig. 1.4.

1.4 The helium atom

The helium atom serves in this work as a benchmark system to investigate electron-electron correlation. Since electrons are *per se* indistinguishable particles, the total wave function $\Psi(e_1, e_2)$ is antisymmetric under exchange of the particles, obeying Pauli's principle. This symmetry already indicates a

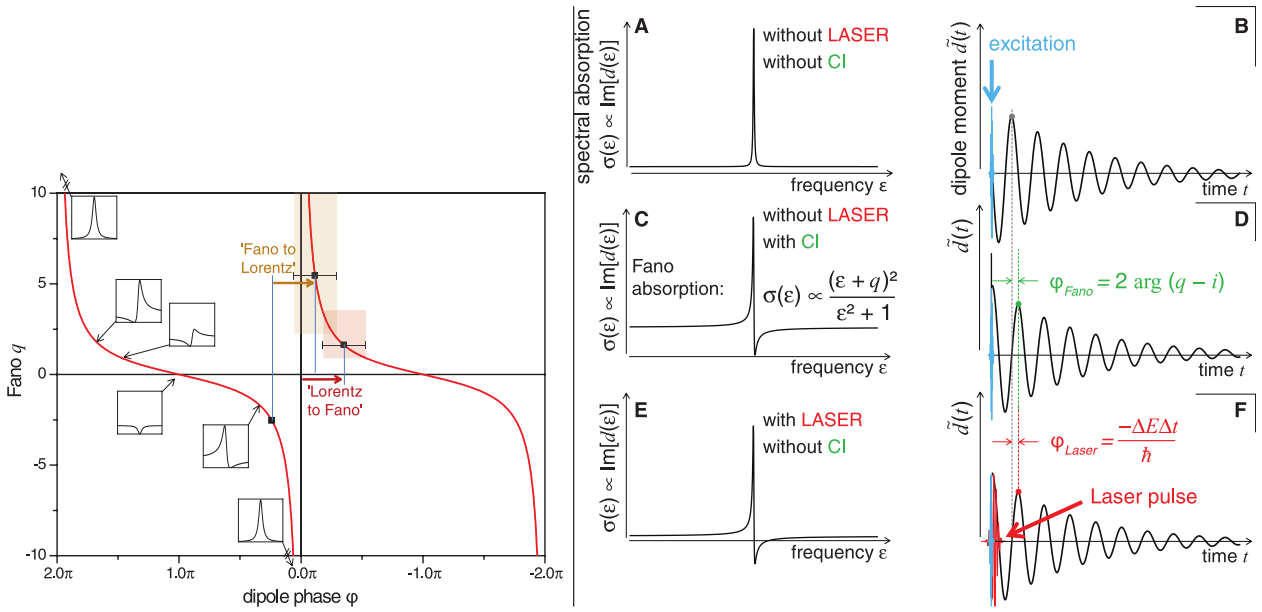

Figure 1.4: **left:** Mapping of Fano's asymmetry parameter q to the dipole phase φ. For $q \to \pm\infty$ and $\varphi \to 2\pi$ the line shape is Lorentzian. For the other extreme $q \to 0$ and $\varphi \to \pi$, the line shape forms the window resonances. In between the characteristic Fano line shapes can be observed. **right:** The dipole response function (B,D,F) of an atomic system after excitation and the corresponding line shape (A,C,E) for different circumstances: undisturbed (top), with configuration interaction (middle), with a laser manipulating the state . Both Reprinted from [2]

correlation between the electrons. The total wave function can be written as

$$\Psi(e_1, e_2) = \Psi(\mathbf{r}_1, \mathbf{r}_2) \cdot \chi(S_1, S_2). \tag{1.42}$$

Both terms, representing the wave functions of the spatial degrees of freedom and the spin respectively, can be decoupled and the latter be disregarded as it has no impact to this work. A state involving two electrons is denoted in the spectroscopic notation

$$^{2S+1}L^{\pi} \tag{1.43}$$

with quantum numbers for the total angular momentum L and total Spin S. For convenience π represents directly the parity of L, with "o" and "e" for odd and even respectively. The doubly excited state of relevance to this thesis, the 2s2p state in helium, is a spin singlet state (S=0) with an antisymmetric spin wave function. Hence, the orbital wave function is symmetric. Furthermore, with

laser-induced dipole transitions the initial and final state must exhibit opposite parities. Since the ground state of Helium ($^1S^e$) is even, only $^1P^o$ states are allowed with single-photon excitation. Since electron-electron correlation is investigated here, the independent particle model and the resulting disentanglement of the spatial wave function into a product of two single-electron wave functions cannot be utilized. The interaction between electrons can be described by the Coulomb force

$$\mathbf{F}_C = -\frac{1}{4\pi\epsilon_0}\frac{e^2}{|\mathbf{r}_1 - \mathbf{r}_2|} \tag{1.44}$$

and is the initial point for several approximation approaches. For auto-ionizing states, the approach of configuration interaction is treated in Ch. 1.3.1. The mixing of single-electron states occurs via the interaction V_E, which in this treatment corresponds to the Coulomb repulsion. A doubly excited state can be identified with the inner and outer quantum number N and n, respectively, in the picture of an uncorrelated product state. The first series in helium of such states shows the quantum number N=2 with a $^1P^o$ symmetry, which allows for the three series 2snp, 2pns and 2pnd. All series converge to the double ionization threshold 65.40 eV. For excitations higher than this, one electron is ionized while the other remains in the N=2 state. The residual energy to the threshold is measured as kinetic energy of the ionized electron. Hence it can be distinguished whether an ionized electron originates from a doubly exited state or a singly excited state with an ionizing threshold at 24.59 eV.

Comparing the three N=2 series, the cross section of these involving the s orbital exhibit a higher cross section as the angular momentum absorbed from the photon has to be distributed only to one electron, while for the third series both electrons have to exchange such momentum with the radiation field. Initially only a strong and a weak series were detected [9], which lead to the approach of a superposition. The linear combination

$$\frac{1}{\sqrt{2}} = (2sn\mathit{p} \pm 2\mathit{p}ns) \tag{1.45}$$

describes the strong "+" and the weak "-" series, abbreviated as $sp_{2,n+}$ and $sp_{2,n-}$ respectively. The 2s2p series belongs to the strong series. The third

series was the weakest and therefore found decades later in high resolution studies with synchrotron radiation, where also the $sp_{2,n+}$ series was investigated in great detail, in particular the line shape and positions of the resonances [10], [11].

The lifetime of an auto-ionizing state ranges from 17fs of the lowest, the 2s2p, up to several 100fs for higher $sp_{2,n+}$ states. The lifetime corresponds to an energetic bandwidth of 38 meV down to a few meV respectively. A short overview about the lowest states is given in table 1.1

	E_r (eV)	Γ (meV)	q
2s2p	60.1503 ± 0.0040	37.6 ± 0.2	-2.74 ± 0.04
$sp_{2,3+}$	63.6575 ± 0.0030	8.3 ± 0.5	-2.53 ± 0.04
$sp_{2,4+}$	64.4655 ± 0.0020	3.4 ± 0.7	-2.58 ± 0.05

Table 1.1: Line shape parameters (cf. Ch. 1.3.1) for the three lowest doubly excited states belonging to the $sp_{2,n+}$ series. Values from [10].

1.5 Free Electron Laser

The idea of a free electron laser (FEL) was invented by J. Madey in the 1970s at Stanford University and realized soon after. Though not limited to the XUV, it presents a coherent light source with tunable, high power and high brilliance radiation in this spectral range. It is based on initial spontaneous emission but otherwise differs strongly from the conventional concept of Light Amplification by Stimulated Emission of Radiation (LASER).

The device is made of three major parts: The photo injector, the accelerator and the undulator. At first, a bunch of free electrons is generated. At FLASH, this happens in a photo injector based on a RF-gun. Here, an optical laser produces photoelectrons from a photocathode. The structure and the timing of the laser pulse determine the equivalent parameters in the electron beam.

The superconducting **li**near **ac**celerator (LINAC) accelerates these electrons to relativistic speeds on the order of 1.25 GeV. Accounting for divergence the electron beam is refocused. Also in order to reach high currents and therefore high charge densities in the undulator the beam is compressed along the propagation axis as well. An increase from 50A up to 2kA can be achieved, which is required for the lasing process. These transversal and longitudinal

compressions take place at intermediate energies (150-450 MeV) between the six acceleration modules with the superconducting cavities. At the end the beam is collimated and passed on to the next section.

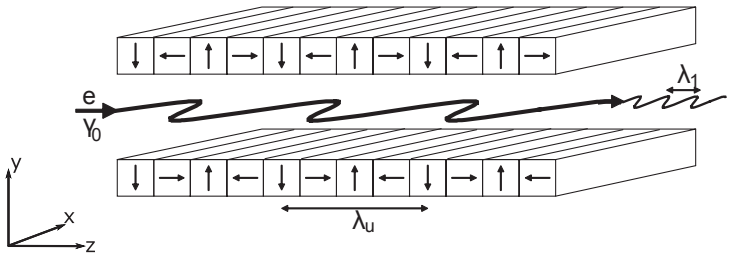

Figure 1.5: Conceptional drawing of an undulator. Electrons travel in z direction and experience the periodic magnetic field in the vertical y direction. They start to conduct a wiggle motion on the horizontal x direction. This leads to the emission of synchrotron radiation. Reprinted from [12]

The process of coherent light generation takes place in the undulator. On a macroscopic scale, the electrons enter this part as a bright electron beam. The undulator itself is a set of two planes of permanent magnets (NdFeB) with peak field strength of 0.47T, arranged in an alternating manner with a fixed gap of 12 mm between the planes and a periodicity of 27mm, see Fig. 1.5. The total length amounts to 27m. The electrons traveling along the z direction in the undulator experience the periodic magnetic field in the vertical y direction and start to conduct a wiggle motion on the horizontal x direction. This leads to the emission of synchrotron radiation as expected by an accelerated charge. The magnetic field can be described as $B_y = B_0 \sin(\frac{2\pi}{\lambda_u} z)$, with the undulator period λ_u. The emitted radiation has the wavelength

$$\lambda_r = \frac{\lambda_u}{2\gamma_0^2}\left(1 + \frac{K_0^2}{2} + \gamma_0^2\,\Phi^2\right) \tag{1.46}$$

with γ_0 the energy of the electrons in unit of the rest-mass energy mc^2, the undulator strength parameter $K_0 \propto B_0\lambda_0$ and the radiation angle Φ in terms of the undulator axis. So far the radiation is emitted spontaneously and not in phase to each other, thus emitted incoherent. This is the initial point to the radiation process. Due to the relativistic energies of the electrons the light is emitted only as a small cone in forward direction. However, only the radiation emitted along the propagation axis is of interest. Hence the angular dependence in Eq. 1.46 is eliminated and Φ set to zero. The resonant

wavelength in forward direction yields

$$\lambda_1 = \frac{\lambda_u}{2\gamma_0^2}\left(1 + \frac{K_0^2}{2}\right) \tag{1.47}$$

During one undulator period the radiation overcomes the electrons by λ_1. Due to the periodicity of the system the electromagnetic plane wave of this radiation is sustained, see Fig. 1.6.

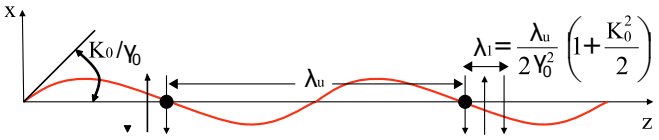

Figure 1.6: While an electron (black dot) travels one undulator period λ_u of the sinusoidal trajectory (red), the plane wave (alternating vertical arrows) overtakes it by one resonant wavelength λ_1. The radiation with this resonant wavelength can therefore exchange energy with the electron over many undulator periods. Reprinted from [12]

Depending on the relative phase of the plane wave and the electrons, some of them gain energy from the radiation while others release energy into the EM field. This leads to a periodic modulated energy density within the bunch. As this assemblage propagates, electrons with higher energy move faster and bunch up with electrons of lower energy further up the beam. The energy modulation evolves into a charge density modulation. This substructure is called "micro-bunching". The spacing of micro-bunches corresponds to the scale of the resonant wavelength λ_1.
With the resonance condition fulfilled the micro-bunches generate coherent light. This process of self-amplified-spontaneous-emission (SASE) allows for exponential gain of the spontaneous emission. As the electron bunches contribute more and more energy to the electromagnetic wave, they suffer loss in their own kinetic energy. Eventually this leads to a violation of the resonance condition. At this point the amplification levels out and the bunching reaches it's maximum, see Fig. 1.7.

In addition to the fundamental mode, harmonics of the 3rd and 5th order, which naturally fulfill the same resonance condition, are observed at FLASH. With this coherent radiation it is possible to perform experiments in the water window between $280 - 530$ eV (4.5 nm), even though with much smaller pulse energy. When it is not desirable to have these harmonics in the spectrum for

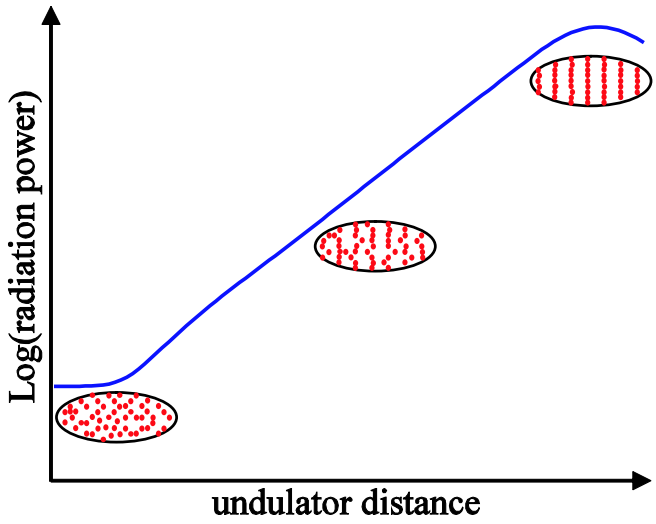

Figure 1.7: Increase of the radiation power and the electron beam microbunching in the undulator over distance for a high-gain FEL. Reprinted from [12]

an experiment, they can be suppressed.

If one was to compare a FEL to a conventional laser, the electron beam would present the active medium and the setup would correspond to a single pass amplifier.

The theory so far would give rise to fully coherent light. Since the electron-bunch generation is subject to shot-noise, the electrons enter the undulator in a stochastic manner. On a macroscopic level the electrons thereby can no longer be considered a contentious beam. This influences many parameters, like the bunching, the temporal structure and the corresponding spectrum. These entities vary from shot to shot and the light is quasi-coherent only. However it provides a high transversal coherence.

FLASH is conceptually a self seeded high gain FEL with a single path undulator. Small gain FEL use optical cavity to enhance the emitted intensity. This has been done mostly in the VIS and IR spectral range. For XUV light it is hardly utilized since the lack of appropriate optical components in this spectral region. Another concept uses seed laser instead of the spontaneous emission to initiate the process of amplification. This is mostly done with a high harmonic source and leads to a narrower spectrum, which can even be tuned within the gain profile of the undulator.

The FLASH on the other hand emits the full spectrum of the undulator's gain profile, but therefore exhibits strong shot to shot noise due to the spontaneous

initiation of the amplification process.

The permanent generation of high intense light leads to damage. FLASH, like many other facitlies is therefore operated in a pulsed mode. With a frequency of 10Hz, a pulse train with up to 400 pulses is delivered, see Fig. 1.8. The pulses within a train are separated by micro seconds, depending on the actual count of pulses. It is possible to reduce this number of pulses by any integer number, allowing for different settings at experiments. In our case the single-bunch mode was usually set, delivering a single pulse every 100ms. For more information on the theory of FELs, be referred to [12][13][14].

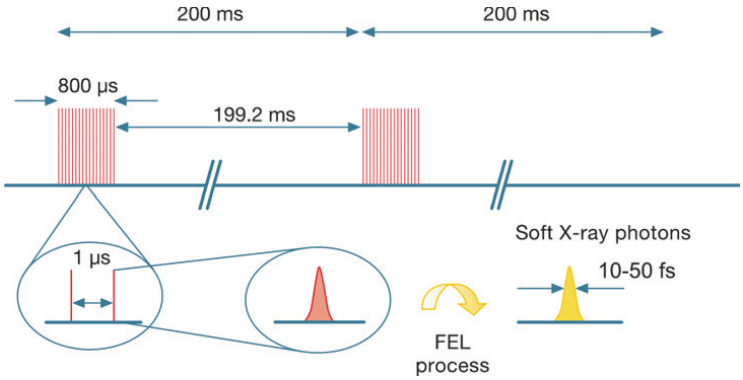

Figure 1.8: Pulse train structure of FLASH. The values on the figure are outdated. It serves only to illustrate the temporal structure of the SASE. The pulse trains arrive with a frequency of 10Hz. Every train consists of up to 400 bunches, separated by micro-seconds. Reprinted from [14]

2 Setup

The experimental setup brought to use at FLASH in Hamburg and the center of this work originates from a tabletop instrument for multidimensional spectroscopy with extreme ultra violet (XUV)/ soft x-ray and visible (VIS) light. A tabletop femtosecond Titanium-doped Sapphire (Ti:Sa) laser provides ultrashort coherent pulses in the VIS region (500-1000 nm). Besides being used later as the pump in a pump-probe scheme for dynamic spectroscopy, these pulses are focused into a gas cell in order to generate high harmonics (HHG). These in turn present the XUV source to the experiment.
As this setup, including the HHG part, was used to test the entire system in the home-laboratory in Heidelberg before being shipped to the free electron laser facility at DESY in Hamburg, this chapter will firstly describe the full experimental setup, including the HHG compartment.
Especially, certain features of the setup will be highlighted, which have been developed in preparation for the beam time itself or been improved following the gathered experience in recent experiments. For example the four-split-mirror and its technical operation will be presented as well as improvements on the filter-unit and the redesign of the target cell system. For more information on other parts and techniques and working principles be referred to earlier theses [6][15].
Secondly, a short layout of the FEL postproduction, especially features being used during the experiments, will be given. Finally the changes to the beamline made for the beam time itself at FLASH will be described.

2.1 HHG-beamline

An overview of the complete experimental setup of the still novel beamline is depicted in Fig. 2.1. Its individual components are presented in the following. For the commissioning in the home laboratory, the setup is provided with

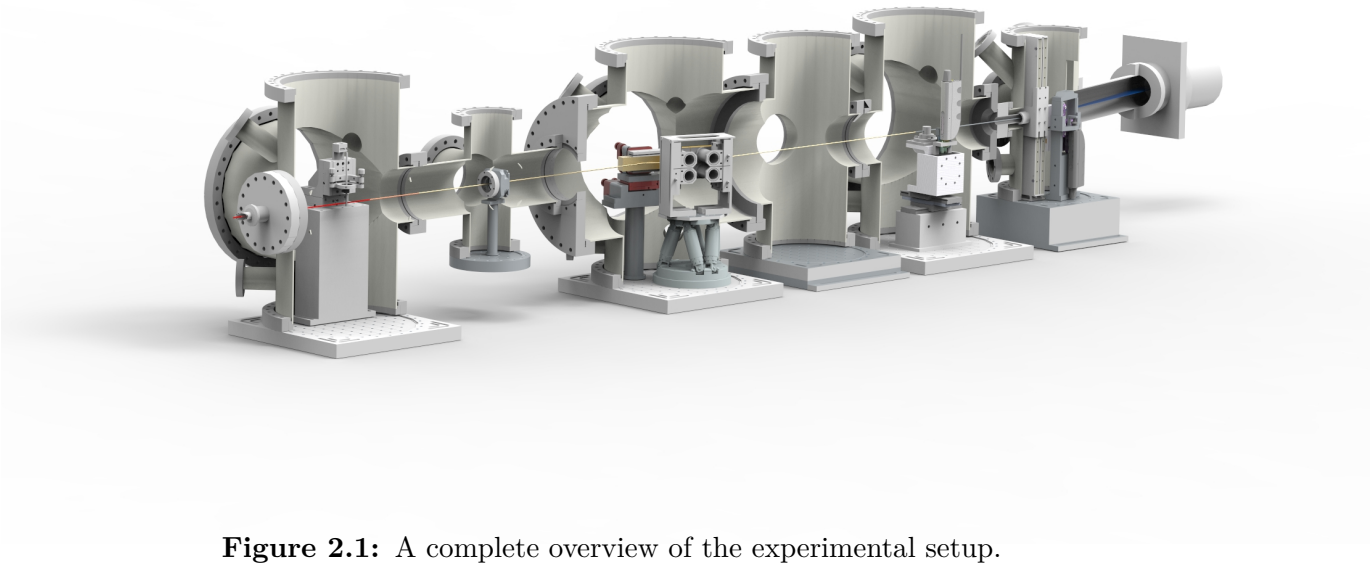

Figure 2.1: A complete overview of the experimental setup.

ultrashort laser pulses with a central wavelength of 760 nm. The pulses possess a nearly octave-spanning bandwidth, allowing for pulse duration of sub-7 fs (10^{-15} s). The high peak intensity of the order of 10^{14} W/cm^2 and the focal spot size of about 50 μm allow to drive highly nonlinear processes, like HHG. The pulse repetition rate of the laser at 3 kHz is much higher compared to the 10 Hz of the FLASH. The beam is coupled into the first chamber, the HHG Chamber, and focused down into a gas cell. This cell is a vertical tube of stainless steel with two 100 μm-holes on opposite sites for the laser to pass through. It is fed with a noble gas like Argon or Xenon at a backing pressure of several tens of mbar. The cell is mounted on a three dimensional translation-stage system to ensure among other things a proper phase matching.
Since the HHG does not present the source to the main measurements performed in this thesis, be referred to [6] for further introduction on the generating process. (The XUV source used instead, is presented in Ch. 1.5 about FELs.) The generated XUV beam is then co-propagating to the VIS beam. The divergence of both beams differs significantly. It is on the order of 15 mrad and 1 mrad for the VIS and XUV beam, respectively.

The difference is exploited in the next camber, which contains a motorized iris aperture. It cuts out the outer part of the VIS beam without influencing the inner XUV. This provides the tuneability of the VIS beam intensity. This device, though hardly used during the course of this work, presents the key feature to a precursor and related experiment of laser controlled absorption line-shaping in Helium [5]. In this work, the same experiment will be discussed, this time with XUV only.

The succeeding Mirror Chamber contains the refocusing optic and the split-and-delay unit. For maximal reflection in a broad band of energies, gold-coated optics under grazing incidence of 15° are used. Dielectric optics provide a high throughput only in a narrow band, limiting the choice of photon energies of the entire setup to this bandwidth and making it a poor choice for broadband HHG spectra.
To image the first focus of the first chamber into the target, a toroidal mirror is utilized. In order to minimize imaging errors, 2f-2f geometry was chosen, providing an imaging ratio of 1:1. With a focal length of f=350 mm this adds up to 700 mm between this optic and both foci.
For alignment, this mirror is mounted on a motorized 5-axes aligner and mirror mount. Ultrashort laser pulses usually do not provide the best Gaussian beam profile due to their generating process. Therefore a laser with a more ideal one, e.g. a Helium-Neon-Laser, is recommended, allowing an alignment with minimal astigmatism. For a tutorial on how to best align this toroidal mirror, be referred to a previous thesis [15].
The split-and-delay unit contains up to four oblong quadrants, mounted in a two by two geometry. As the beam hits the mirror, it is ideally split in up to four identical copies, the absence of a spatial chirp presumed. In order to minimize the loss due to the gap between the mirrors, they are mounted as close as possible together with a distance similar to 200 μm.
The first mirror is fix and employed as the local oscillator (LO) in a two dimensional absorption spectroscopy type of experiments. The remaining mirrors are each mounted directly on a delay stage, providing a travel range of 250μ m with a nominal precision of 1 nm. The individual positioning of each mirror perpendicular to their surface induces the delay between the pulses and is therefore the key feature of dynamic spectroscopy. Under grazing incidence of 15° the travel range translates into a total delay of 430 fs with a resolution

of about 2 as. As vibrations induced by the turbo molecular pumps and other circumstances decrease the resolution of the stages, a lower resolution on the order of tens of attoseconds is expected. Since the main focus of this work, besides the construction of this setup for FLASH, is a static spectroscopy experiment, the stability will be no further investigated here.
Furthermore, a tip and tilt stage is directly connected to each mirror. This provides an individual high precision tilting ability of 5 mrad with a precision of 0.05 μrad. This becomes necessary when a delay stage is set to distance on the order of to the spot size in the focus. In this case the overlap of the beams with the target volume diminishes significantly or shifts completely out of it, see Ch. 2.1.1.
To compensate for that, the tip tilt stage is used to restore the overlap in the target cell, where the target volume is defined. During the experiments a correction of about 0.5 mrad for a full delay of 430 fs was found. Further details on how this correction was implemented are outlined below, Ch. 2.1.1.
In order to account for different conditions at the FEL or to run different kinds of experiments without bigger efforts, the four-quadrant split mirror is mounted on a Hexapod, a high precision stage with 6 degrees of freedom. This enables to quickly react to changes in beam pointing as well as changing the number of mirrors illuminated. Also the intensity ratio between the individual segments can be adjusted easily.

Between the mirror chamber and the target chamber a reference spectrometer is planned to be integrated. This option gives the opportunity to simultaneously measure a reference spectrum to the signal from the target on a shot-to-shot basis. It enables to filter out spectral characteristics of the light source, as for example the harmonic structure, and directly calculate the optical density. Therefore results from techniques like the Fourier filtering or the use of reference spectra on the main detector without target, which are susceptible to errors due to drifts and jitter in the light source, can be avoided. For the commissioning in Heidelberg, such a spectrometer was not necessary, as for the experiment performed at FLASH, the reference spectrometer on-site was used.

The adjacent chamber contains the target. Since our goal comprised also, though not subject of this thesis, the measurement of halogenated hydrocarbon molecules, e.g. Diiodomethane, which is in liquid phase and shows a very small vapor pressure of about 1.5 mbar at room temperature, the heating of the

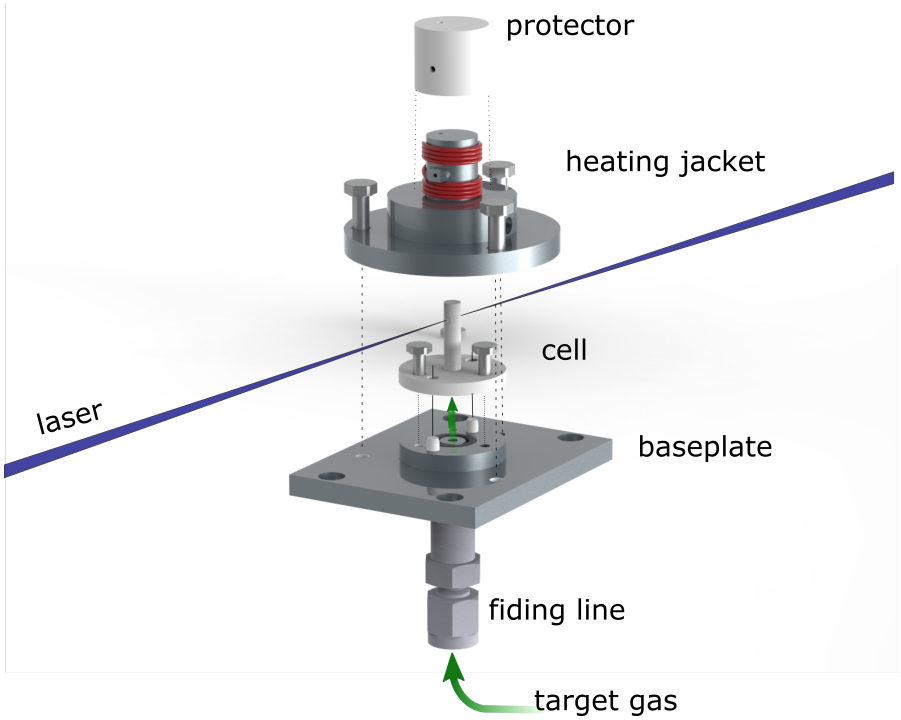

Figure 2.2: The new designed target cell. It consits of three parts baseplate, cell and heating jacket. It is designed to withstand longer to VIS laser and for fast assembly. The dowel pins in the baseplate make realignment obsolete. It is mounted and a fast three axis translation-stage system with high precision.

supply line and the target cell itself needed to be considered.
Furthermore, also the possibility of clogging of the cell had to be faced. Especially critical at the 100μ m small entrance holes on the beam axis, these molecules start to polymerize when ionized by the intense FEL radiation. Since the exchange of the target cell in the old design, similar to the HHG cell, is quite time-consuming and time during FEL-beam delivery is of high value, an entire new cell system was designed.
The new cell, see Fig. 2.2, basically consists of three parts. The baseplate provides the target gas from a feeding pipe beneath and is mounted to the stage positioning system. The cell itself is a vertical cylinder of 2 mm inner and 4 mm outer diameter with closed top and two holes drilled on opposite sides. The interaction volume is defined between these two 100-200μ m holes, which are aligned along the beam axis. The cell was produced in two kinds of materials, stainless steel and macor ceramics. The latter one is known to withstand longer to intense focused beams in the near infrared (NIR) and VIS spectral range. The stainless steel version is more prone to laser ablation,

leading to the necessity of a higher gas flow, resulting in a higher pressure in the target chamber.
However, at the FEL, the stainless steel version was implemented due to higher experiences with this combination. The last part is the optional heating jacket, which provides the uniform heat to the cell. A shield prevents damage by the laser beam to the heating wires wrapped around it. These wires provide the necessary heat, up to temperatures of 130°C. The jacket as well as the feeding system is monitored by several thermal sensors, which are connected to the thermostats driving the current in the heating wires. As the different parts are simply stacked onto each other and fixed by very few screws, the cell dis- and assembling is very comfortable and fast. In order to avoid the realignment of the cell to the beam axis at every exchange, dowel pins in the baseplate restrain the cell always back into the same position.
The entire cell complex is mounted on a 3 axis translation stage system. It is also optimized for high speed and also high resolution alignment, as the focus can exhibit a spot size of just 20 μm and Pico-motor actuators have been proven too slow for this task. Velocities up to 20 mm/s and 1 mm/s can be reached for the horizontally and vertically axes respectively and resolutions of 10 nm and 1 μm respectively are achieved. Furthermore a scintillator screen is mounted next to the cell, to allow alignment in the focus and finding the overlap of the split beams. The stage is fully extractable from the beam path to enable a hybrid ToF with repeller to be placed in the beam.

The final chamber represents the spectrometer. It consists of a filter unit, a variable line spacing grating (VLS) and the XUV detector. The filter unit at the entrance blocks the light in the VIS regime. Since these frequencies are not part of the probe of core level interactions, they would scatter within the chamber and blur the result as background noise. Also strong XUV light after the target is attenuated here, to preserve the detector chip from saturation and damage. The material of the filters, e.g. Al, Zr, In, is chosen to fulfill these demands with their spectral profile and an adequate absorption with thicknesses between 200 nm and several μm.
In earlier setups difficulties occurred from leakage of this unit, resulting in a high background noise. This was improved in a completely new design, which shall be briefly presented. To prevent any leakage from entering the chamber the key method during the design of the unit was the establishment

of physical overlap. No two interfaces were to be connected just to each other without forcing the irregular light to be scattered around at least another corner. The filter unit hence is connected directly on the differential pumping stage, through which the beam enters the chamber.
As the filters exhibit certain imperfection in the surface by the production process, they itself exhibit a leakage as well. To compensate for this, two filters with the same sum-thickness are mounted consecutively. The statistically distributed nano holes in both filters, causing this leakage, are then most likely no longer on axis. No direct radiation is transmitted unfiltered.
On the other hand, the very small thickness of the filter makes them prone to rupture. As a consequence the volume between such concatenated filters has to be connected very well to the volume of the chamber. This guarantees a minimal pressure difference between both volumes, when the chamber is evacuated and thereby prevents destruction of the filters.
To provide higher flexibility in filter thickness and material in order to account for different circumstances during measurements, not only one pair of filters was aspired.
These demands resulted in a more complex design of the unit, when compared to the previous one. It is depicted in Fig. 2.3. Apart from one filter position, which must be kept empty to account for the pressure difference between the chambers during evacuation, seven filter positions are available on a rail, sliding up and down within its housing. Since the lower one stays fixed in the chamber when filters need to be exchanged, no alignment is necessary when it is put back in. As the rail can be pulled into the upper housing, the filters, old and new, are protected from rupture due to the movement in air during the transport from the chamber to the assembly area. At FLASH, two of these units where used consecutively, assembled with a set of thicker and thiner filters respectively.
At the center of the chamber a reflective variable line spacing (VLS) grating is positioned. It disperses the different wavelength through the detector arm onto the detector. The feature of this concave grating is the refocusing of the first order onto a flat field instead of a focus curve, known as Rowland circle. This enables the detector chip, which is placed on this plane, to detect all energies over its entire length with the same high resolution. Since the VLS grating is optimized for the certain energy region of 20 eV to 120 eV, corresponding

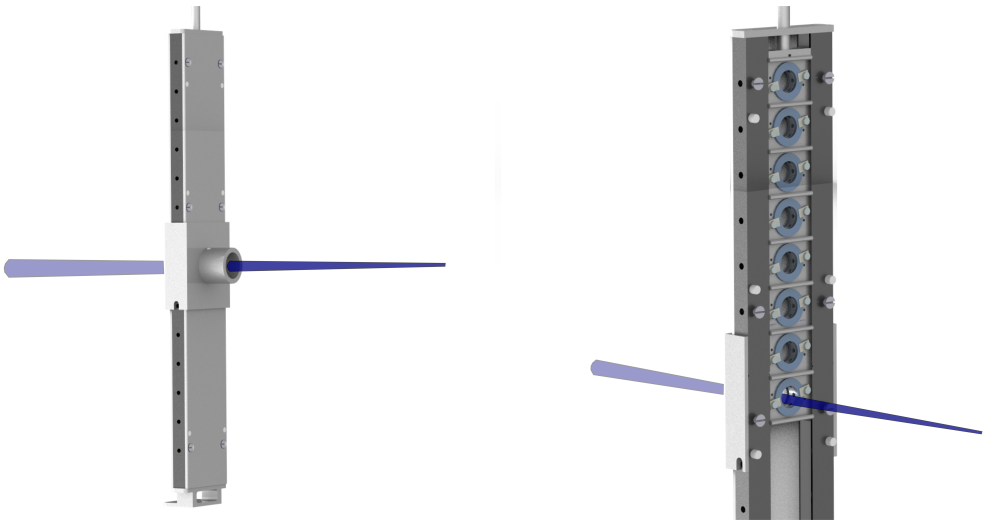

Figure 2.3: The new designed filter unit. Left: it is closed as used in the experiment. The nozzle is mounted directly onto the pumping stage extending into the spectrometer chamber. Right: A cut of the filter unit to look at the components inside. The rail in the center provides seven positions to mount filter on both sides, while the eights position is kept empty for the evacuation process. It can slide up and down to place the required filter in the beam. The lower part including the nozzle holder stays in the chamber to prevent realignment while the upper part serves as transport housing for the filters when extracted form the chamber.

to 62 nm to 11 nm, it is mounted on a motorized vertical stage. This way, a second grating can be used to observe a different energy region without having to re-align the entire spectrometer. The alignment as well as the stability of the stage is crucial to achieve resolutions in the lower tens of meV. Also, in case the quality of a spot where the beam hits the grating's surface has degenerated, it can be easily be shifted. The beam is then moved off this spot. It can further serve as a diagnostic tool during commissioning to identify the origin of structures on the beam profile. This can happen without effort and can even be done to check for such degeneration to begin with.
The XUV-detector, a backside-illuminated XUV-CCD camera, provides 1340x400 pixel with an effective size of 20 μm per pixel. As the camera chip can therefore observe only 27 mm of the 110 mm long flat image plane of the grating, the camera is mounted on a mechanical bearing. This enables to position the camera, named PIXIS hereafter, along the entire field axis. The camera can be peltier cooled down to $-30°$C for electronical noise reduction. It also provides the ability for external trigger synchronization, which is necessary to perform single shot measurements at FLASH.

2.1.1 walk-off correction

The purpose of the split-and-delay unit is time-resolved spectroscopy. Depending on the method, e.g. pump-probe, 2D or 2D phase-resolved, two or more pulses with tunable time delay are required. In this setup these beams are created by a split mirror, producing identical copies of the incoming pulse. As one of the plane mirrors is moved perpendicular to its surface, a temporal delay is introduced relative to the other pulses. All beams are brought into overlap in the target volume, corresponding usually to the volume inside a target cell or above a nozzle.

For the case of grazing incidence, a time delay resulting from a translation distance of the mirror much smaller than the transversal extension of the target volume is uncritical to the measurement. For longer translation length the focus of this beam starts to shift out of this volume transversally as well as longitudinally. The longitudinal walk-off can be disregarded in our case since the Rayleigh length of a few mm is much longer compared to a longitudinal focus shift of tens of µm. The transversal walk-off on the other hand is in the order of and proportional to the translation length ($= \cos(\beta) \cdot d$) and has to be corrected. Tilting the mirror brings the focus back into the target volume. The required angle can be easily calculated using the geometric properties of the setup. For the results to be accurate, highly precise measurements of distances and angles of all objects involved are necessary. These measurements are rather difficult to make with the precision demanded inside a vacuum-chambers-setup. They also have to be repeated after every change to the mirror setup's position. As a consequence a different approach was chosen.

On the distance D of about 680 mm between the mirror setup and the target volume an angle α introducing a 0.250 mm shift d is very small, see Fig 2.4. In this regime the relation between the angle and the mirror shift d can be

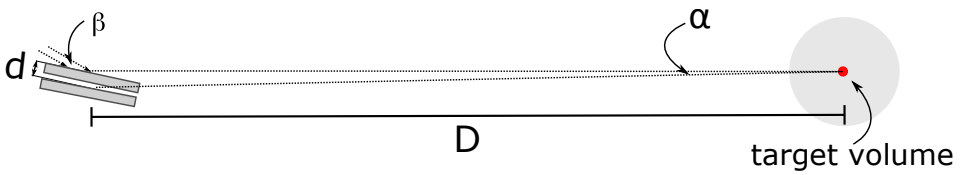

Figure 2.4: Schematic of geometric optic in the vacuum chambers between the split-and-delay unit and the target. The angle between the beams of different delay is small enough that the trigonometric functions can be approximated linearly. Relative deviation $< 10^{-6}$.

assumed linear (relative deviation $< 10^{-6}$). The angle correction required at the mirror corresponds to $\alpha/2$.
At the beginning of a measurement series, a target volume is defined. This is usually the inner part of the cell on the beam axis in the focus. Since the focus can be smaller than the cell, one defines a spot within this area as the target area. It should be considered that a fixed mirror, e.g. LO in 2D-Spectroscopy, is aligned on this area at first, since it cannot be adjusted individually. Furthermore the tip-tilt-units should not be at their end-stops when aligned on this area, to allow the travel range for the following correction. To align the beams in the defined spot a scintillator screen (Phosphor P43) or CCD chip can be utilized.
Once defined, both end stops of the delay unit are approached. Each time the tip-tilt parameters are adjusted in a way that the focus is restored to the target spot. The adjusted parameters are recorded and a linear function is fitted in dependence of the delay position. Whenever a delay stage is set to any number between the end stops, the new parameters are calculated from this fitted function for the respective tip-tilt unit. This compensates the walk-off sufficiently.
The processes described above are implemented in the user-interface, a home-built Labview 13 program, controlling the entire mirror setup. The user establishes the overlap of the beam with the target spot. This can be supported by separate homemade diagnostic software. By activating the program sequence, the processes of recording, interpolating, and adjusting the stages is executed automatically. The method is also independent of the number of mirrors since only the overlap with the self-defined target area is of relevance.

2.2 FLASH photon diagnostics

The working principle of a Free Electron Laser is described in chapter 1.5. Since the amplification process of the FLASH starts with spontaneous emission in the electron bunch, the delivered SASE is subject to stochastic behavior. In consequence, every photon pulse differs strongly from the preceding in terms of pulse energy and temporal structure, which is in turn connected to the spectrum, but also in terms of beam pointing. To perform high precision experiments, this gives rise to the necessity of a variety of photon diagnostic

tools, monitoring such parameters in parallel to the user's measurements and therefore non-destructively. In the following the experimental hall of FLASH with the interior shall be discussed shortly and a few of these devices, which were essential to our campaign and especially to the measurements discussed in this thesis, shall be highlighted. A schematic overview of the FLASH experimental hall is given in Fig. 2.5 After the linear accelerator and the

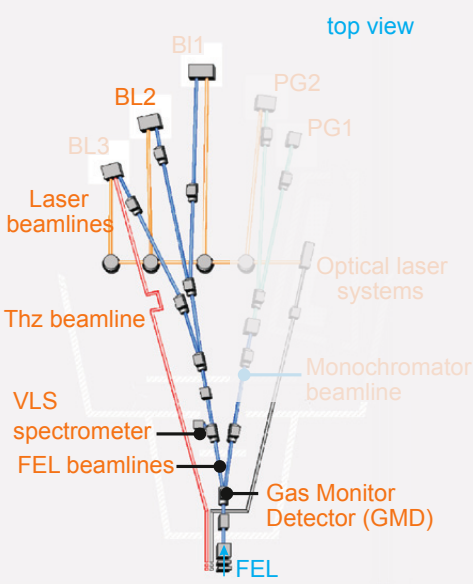

Figure 2.5: A schematic overview of the experimental hall at FLASH. This figure is modified and reprinted from [13]

undulator a dipole magnet diverts the electron bunches off the photon beam axis.

After another 30 m the beam reaches the experimental hall. Before entering the open hall, the beam passes through a gas monitor detector (GMD).

The chamber of this GMD (Fig. 2.6) is filled with a very dilute gas. The beam ionizes the gas and generates ions and free electrons. Two electrodes, namely Faraday cups, collect and detect the charged particles. The resulting current is proportional to the beam intensity, which in turn integrated over the duration of one pulse yields the pulse energy. It ranges, depending on the global settings of the FEL, between 1 and 500 μJ per pulse. Since the electrons move very fast, especially compared to the ions and their higher weight, it is possible to resolve single shot pulse energy. The total accuracy is at about 10% though.

Directly after the two electrode cups two sets of split electrode plates are located,

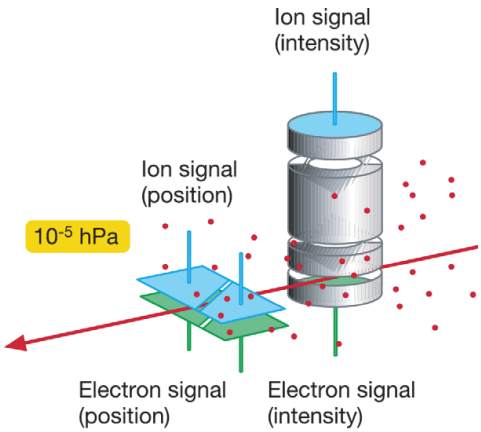

Figure 2.6: Schematic of a Gas Monitor Detector. The right part evaluates the intensity of the beam while the left part determines the beam pointing. Reprinted from [14]

one horizontally and one vertically. These serve as a position monitoring tool. Instead of measuring the absolute current from the electrodes, the ratio between the different sides is being evaluated. Due to the geometry of these plates, as can be easily understood from Fig. 2.6, this enables the determination of the beam position. The gas used as the ionizing target is chosen such, that no resonances are in the surrounding to the currently delivered SASE wavelength. In combination with a pressure of about 10^{-6} mbar, this device leaves the photon beam unaltered and does not reduce its flux significantly.

After the GMD a gas-absorber is located. This device serves as a user controllable attenuator. It is a 15 m long gas tube filled with a noble gas or nitrogen, depending on the wavelength of the SASE in analogy to the GMD. Here for example nitrogen is used for a wavelength of 19-60 nm. Xenon or Krypton can cover the range of 9-19 nm. In order for the attenuator to be nondestructive to the beam, differential pumping stages were used at both ends of the tube instead of windows. The variable pressure, which is applied within minutes, can be used to increase the density of absorption targets for the photons. This reduces their flux and therefore the pulse energy without changing the spectral profile. It was also found that this method even preserves the quality of the wave front and therefore the coherence of each pulse [14].

At the entrance to the experimental hall, the beam passes another GMD. Both GMDs in combination deliver the full set of information in terms of

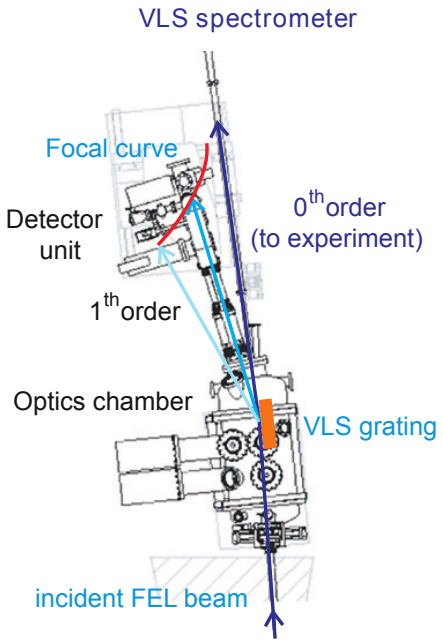

Figure 2.7: Schematic of the on-site reference spectrometer at FLASH in the beam distribution line. The zero order of the variable linespaceing grating (VLS) is transmitted on to the end-station while the first order is recorded as a reference spectrum on a scintillator crystal. Reprinted from [13]

beam pointing, namely position and angle, and the intensity, reduced by the gas-absorber.

The beam is then distributed onto one of the two branches and their connected end-stations. The mirrors used to distribute the beam are irradiated under a gracing incident angle of $2 - 3°$. The water cooled substrates of 0.5 m silicon have carbon coatings and show a roughness of about 0.5 nm. This results in a reflectivity of about 95% below 200 eV, which contains the FLASH fundamental modes. The length of the optics and hence the spot-size on their surfaces provides a high damage threshold when high pulse energies or long pulse trains are delivered.

The 'monochrome' branch, denoted with the acronym PG, serves two end-stations. On the way the beam passes through a high precision monochromator containing a plane grating (PG). This delivers light with a very small bandwidth ($< 10^{-4}$). Since our goal is time resolved spectroscopy, short and also intense pulse are essential. Monochromatic spectra on the other hand allow only for

longer pulse duration, limited by the Fourier-transformation. These beamlines are mainly used for Raman-spectroscopy or spectroscopy of highly charged ions.
The 'direct' branch serves three beam lines, abbreviated simply with BL. They deliver the full spectral bandwidth of the FLASH and hence offer the for our experiment necessary spectral bandwidth and shortness of pulse duration. It is generally utilized for absorption spectroscopy to resolve the precise spectral line shape but also miscellaneous scattering experiments.
The full spectrum on the other hand, in combination with the jitter due to the generation process, demands an online monitoring spectrometer. Since most users don't implement one of their own, the FLASH facility provides an on-site spectrometer located in the beam distribution array. This spectrometer is conceptually similar to our spectrometer. It is based on a VLS grating. While the first order is used to record the spectrum, the zero order reflection is passed on to the end stations. This technique is key to actually record the spectrum simultaneously to the measurement.
The first order is irradiated onto a scintillator crystal. A detector-camera (PCO) records the spectrum, see Pic. 2.7. Lately, a second detector (Gotthard) has been installed in addition. It observes the crystal from the back side. In multi-bunch mode this detector enables to not only observe with the 10 Hz repetition rate an accumulation of the pulse train, but to record single pulse spectra within the train. The payoff is a limited spatial resolution to only one pixel in the direction perpendicular to the dispersion plain of the grating. Since most of our experiments were performed in the single bunch mode, it was hardly made use of this device.
Further devices are located along the beamline, for example filter wheels and apertures. The filter serve as discrete attenuators in a more static fashion, compared to the gas-absorber.
To identify the recorded data of the various devices an ongoing integer number, called BunchID, is assigned to every pulse-train deliverd by the FLASH. This way, the spectra recorded in our measurement can be connected to beam parameter, allowing for sorting and filtering the pulse by certain criteria as well as calculating values like the OD.
To account for minimal absorption during the beam delivering, the pipe system

is held under UHV (10^{-9} mbar)
Our setup was hooked up at the station BL2. This station is equipped with a 2 m elliptical mirror, focusing the beam down to 20 μm (FWHM). For the experiment discussed in this thesis a photon energy of 60.15 eV was set which is equivalent to 20.61 nm. Average pulse energy of about 60 μJ with peaks up to 120 μJ was recorded.

2.3 Beamline modifications at FLASH

As the experiment moved to Hamburg, the XUV light generated in the HHG chamber was no longer necessary. The chamber with its cell was still left inside though, as a backup, which did prove very helpful in the course of the campaign.
The focus point defined by the BL2 ellipsoidal mirror is 527.5mm after the connecting flange of the FELs beam-delivery. Since this distance was too small to provide space for half a target chamber, a chamber for the split-and-delay unit and an appropriate number of pumping stages, the refocusing scheme was still implemented. Never the less, further changes were performed.
In order to keep the FLASH beamline independent of our experimental conditions at 10^{-9}mbar, two chambers were added ahead of the HHG chamber. Each of them was assembled with a differential pumping stage and beam diagnostic. The chambers containing the motorized iris and potential reference spectrometer were replaced. They were equipped with a set of mirrors to couple in and out an external laser before and after the mirror chamber, respectively. This served as an extra set of diagnostics for the split-and-delay unit. The extracted iris served as a pinhole for alignment in the mirror chamber.
Since this was our first experiment at an FEL, a high number of diagnostic tools was chosen. These tools mentioned above are apertures, painted with a scintillator substance (Telefunken powder) to make the transverse modes of the beam and especially its shoulders visible to the human eye.
The high number of pumping stages accounted for the high pressure of up to 10^{-3} mbar in the target chamber while the other compartments of the setup are supposed to remain at very low pressure to limit absorption of the beam and to protect the optics from corrosive targets.
At last a chamber between the target chamber and the spectrometer was in-

troduced. It contained a 2D-slit. Since the intensity of the FEL (10^{14} W/cm^2) is much higher than that of our HHG source (10^{12} W/cm^2), the distance of the spectrometer to the target chamber was increased. This provided the space for the chamber. Due to the divergence of the beam only a fraction of it could pass the filter aperture and enter the spectrometer. The 2D-slit with its vertical slit then served as a new entrance slit for the spectrometer, which was formerly fulfilled by the point-like target volume itself. This allowed for high resolution of the VLS grating, since due to its curvature it presents an imaging optic. Furthermore, the width of the horizontal slit did reduce the intensity upon the spectrometer even further. The resulting intensities did not reach the destruction threshold of the filters in the spectrometer.

3 Experiments

The main goal for the beam time at the FEL FLASH in Hamburg was time resolved transient absorption spectroscopy of halogenated hydrocarbon molecules. Hence, the previous chapter covered the design and construction of the beamline with all the details to accomplish this goal.
To achieve a better understanding of the setup and the FLASH, experiments on the well understood benchmark system Helium were performed at the beginning. Among other, a calibration of the intensity was conducted. This measurement, an intensity scan with (partially) coherent highly intense XUV light, is scientifically the central part of this thesis and will be analyzed in this chapter.
First, to get a better understanding of influences of different characteristics of FEL light and the thereby induced effects, the multiple steps of data evaluation are being discussed here. Also, the characterization of the FLASH beam and the on-site measurement devices will be shown. Finally, the measurement in form of the optical density will be presented. It will be fitted by a Fano-profile and the fitting parameters will be discussed.

3.1 Characterizing FLASH-parameters

The mechanisms of the generation of coherent light in FELs were described in Ch.1.5. It is based on a spontaneous process. As a consequence not only the pulse energy varies strongly from shot to shot but also the spectrum of each pulse.
In Fig.3.1 a set of 20 consecutive pulses is depicted. The single spectra differ strongly from each other as well as from their average. To determine how many shots have to be accumulated to obtain a smooth profile Fig. 3.2 shows a set with different numbers of averages. For numbers in the lower tens, the average spectrum still appears very spiky. As the number of accumulations

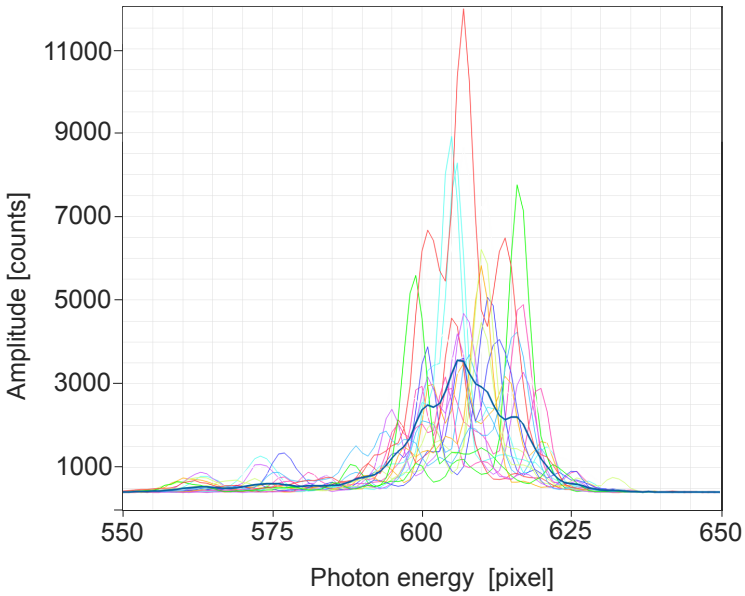

Figure 3.1: Single shot FEL spectra of 20 consecutive pulses (color) in a reference measurement and their average. (thick, blue)

reaches 80 frames, the spectrum with a Gaussian like profile is still not perfect but becomes suitable for our kind of measurements. Hence, a default value of 100 shots per measurement step was set.

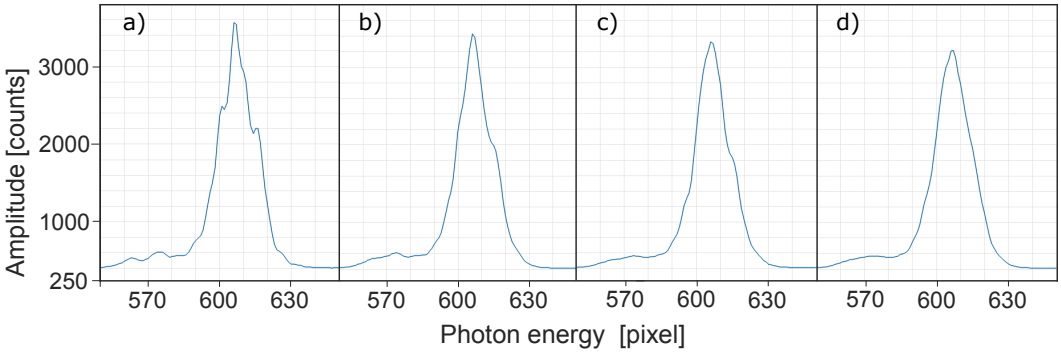

Figure 3.2: Averaged FEL spectra containing 20 (a), 40 (b), 60 (c), 80 (d) pulses.

In terms of pulse energy, most pulses were within a band of 40µJ centered at 60µJ. However pulses providing considerable lower and higher energies were detected as well, see Fig. 3.3.

The origin of these deviations is in the generation process, which impacts also other parameters like the beam-pointing as well as the spectral characteristics and hence the temporal structure. The deviations can therefore indicate aberrations in these parameters as well. Consequences can be a decreased

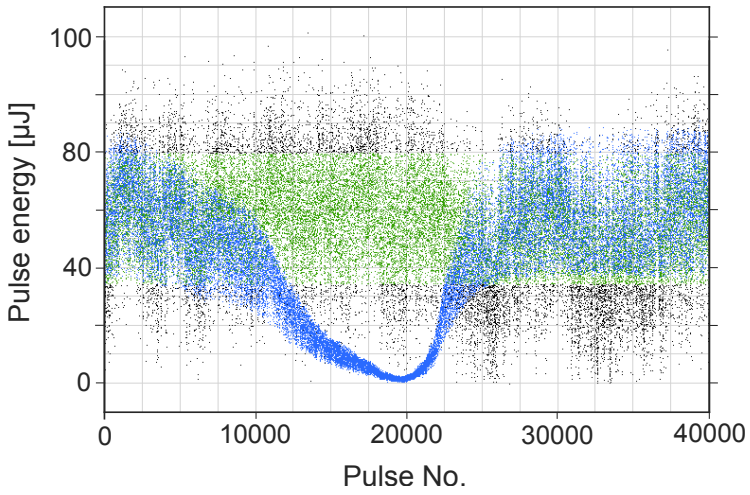

Figure 3.3: Pulse energy recorded by the GMDs before (green+black) and after (blue) the gas-absorber, while the intensity scan with 40000 pulses was performed. Of the incoming pulses the inner 70% about the average energy was utilized (green) while remaining values (black) were excluded from further analysis as described.

focusing due to a misaligned angle on the ellipsoidal mirror. Also different pulse characteristics in time domain can change the experimental conditions in the cell. In the end totally different physical effects can occur which blur out or distort the intended measurement. The exact correlation and analysis of these parameters with the pulse energy is beyond the scope of this thesis. Since a slight improvement of the signal-to-noise ratio could be seen when pulses within the lowest and highest 15% of pulse energies were excluded from the analysis (Fig. 3.3), further investigation of statistical filtering appears to be promising.

3.2 Rescaling of reference spectrometer

The optical density (OD), also known as absorbance and described in Ch.1.1, is the observable commonly used in transient absorption spectroscopy. It is calculated by the negative logarithm of the ratio of the absorption and reference spectra.

$$OD = -log_{10}\Big(\frac{\Phi}{\Phi_{ref}}\Big) \tag{3.1}$$

As indicated before, the here required reference spectra were recorded by the on-site spectrometer in the beam distribution lines. Though similar in the working principle, the two spectrometers and their recording parameters differ immensely.
Illuminated with the same beam, they differ in count rates due to different sensitivity, but also in the position and scaling of the energy axis on the CCD-chips. The correlation of the latter were assumed to be generally nonlinear but proofed linear in the region of interest, see Fig. 3.4. The mismatch originates from different geometric relations in position and angle in the spectrometer setup. The amplitude was assumed to exhibit a linear relation.
Further deviations which cannot be solved by simple rescaling originate from spatial chirps of the beam, which cannot be ruled out. As the beam continuous to propagate through the distribution lines after the reference spectrometer, it passes several filters and apertures. When a spectral chirp exist, they cut out not only part of the intensity but change also of it's spectrum. The Filters meanwhile are chosen such that the transmission function leaves the FEL spectrum unaffected. As a consequence, single spectra did not qualify for the following process, since they differ too strongly in both spectrometers.
To compare both spectra correctly and utilize them for calculations in (3.1), they need to be resampled onto each other. For this process a reference measurement was performed. Several hundred single-shot spectra were recorded simultaneously in our setup without any gas target applied (Pixis) and in the reference spectrometer (PCO). Fig. 3.5b) shows both averages of these spectra.

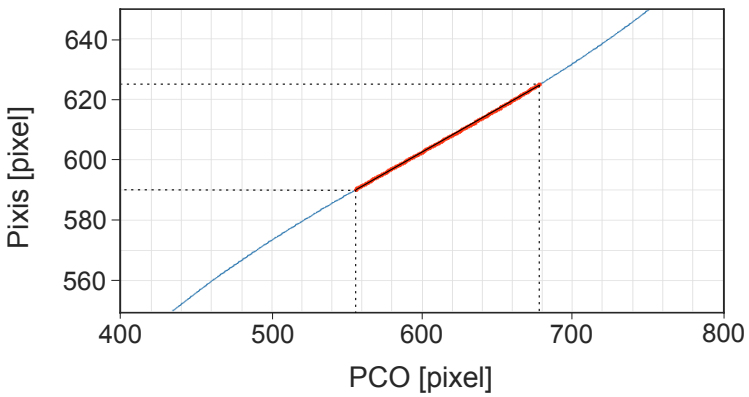

Figure 3.4: The resampling curve of the PCO to the Pixis, zoomed in to the region of the FEL spectrum. The red line indicates the interval used for further calculations in Ch.3.4, which is proven to be linear by the black fitted line.

Then the resampling was performed. A routine using the Levenberg-Marquardt algorithm fitted the PCO spectrum to the background deducted Pixis spectrum with lowest mean square, by rescaling both axes. The resulting spectra were interpolated and projected onto the discrete energy axis of the Pixis. It was chosen to perform the resampling from the PCO to Pixis since the experience with the setup's own spectrometer had been higher. The Result is shown in Fig. 3.5a).

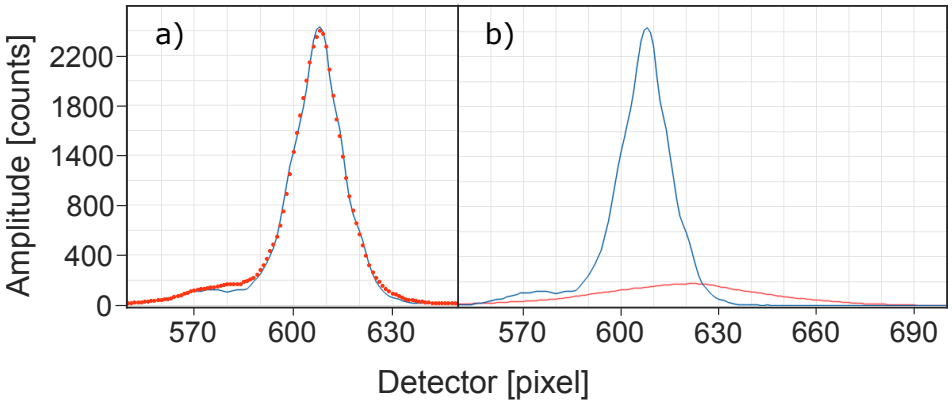

Figure 3.5: Example to illustrated the purpose and the quality of the resampling process. Spectra recorded during a reference measurement with the Pixis (blue) and the reference spectrometer PCO (red). b) presents the data as measured, while a) shows the resampled PCO spectrum on the original Pixis spectrum.

In the experiment an intensity scan with helium was performed. The pulses were attenuated in the gas absorber off-resonantly, so ideally the spectral distribution was unaffected.
However, to prevent the influence of a dynamic parameter, the gas pressure of the absorber in this case, from spoiling the results via incorrect resampling, the procedure was repeated for different pulse energies as well. A reference intensity scan was recorded for this purpose. The pulses were sorted by their pulse energy measured with the Gas-Monitor-Detector (GMD) after the absorber into a histogram with a bin size of 1µJ. The spectra corresponding to the pulses in each interval were averaged in both spectrometers. Then, the resampling was performed for all of these intervals. The resulting resample parameters, shown in Fig.A.4-A.6. They exhibit a constant or linear behavior with very small slope. Especially the 2nd and 3rd oder of the energy axis rescaling exhibits values in the $10^{-}4$ and $10^{-}6$ regime. Hence, the relation of both spectrometers can be assumed to be linear in the energy axis in this spectral range. For pulse

energies greater 45μJ the resampling parameters show strong noise. The reason for this is unknown to this point. Though a too low statistic can be excluded as a origin since the count of bunches during the reference measurement is equivalent to the region around 20μJ, see Fig.A.3. The parameters were fitted linearly to achieve systematic resampling, which was then taken as a basis for all further resampling processes conducted. For the parameters exhibiting the noise the fit was limited to pulse energies below 45μJ and was extrapolated for the region above. The quality of the resampling is equivalent to Fig. 3.5.

3.3 Measurement of double excited states in helium

To compute the optical density of the helium intensity scan from the measured data, a few processes had to be performed ahead. The pulses relevant to the measurement were identified by their BunchID (see Ch.2.3) and recorded in a datalog-file on the experiment computer. With these ID's the corresponding data of both GMDs and the PCO-spectrometer were extracted from the (Hierarchic Data Format) HDF-files provided by FLASH. The correlation of the data from the two spectrometer and therefore the viability of the BunchID concept is proven in Fig.A.2.
The photon diagnostic devices at FLASH sometimes skip the recording of a pulse. The according Bunch-ID had to be filtered and removed from further analyze. The same holds true for pulse trains containing more than one pulse, as the experiment was conducted in single-bunch mode and a double pulse would alter the results. As lined out in Ch. 3.1, pulses with energies far off the average were excluded as well. Then, the Bunch-IDs were sorted in a histogram in dependence of their pulse energies behind the attenuator. After subtracting the background for each spectrum (Pixis), the average for every histogram step was computed. The result is depicted in Fig. 3.6.

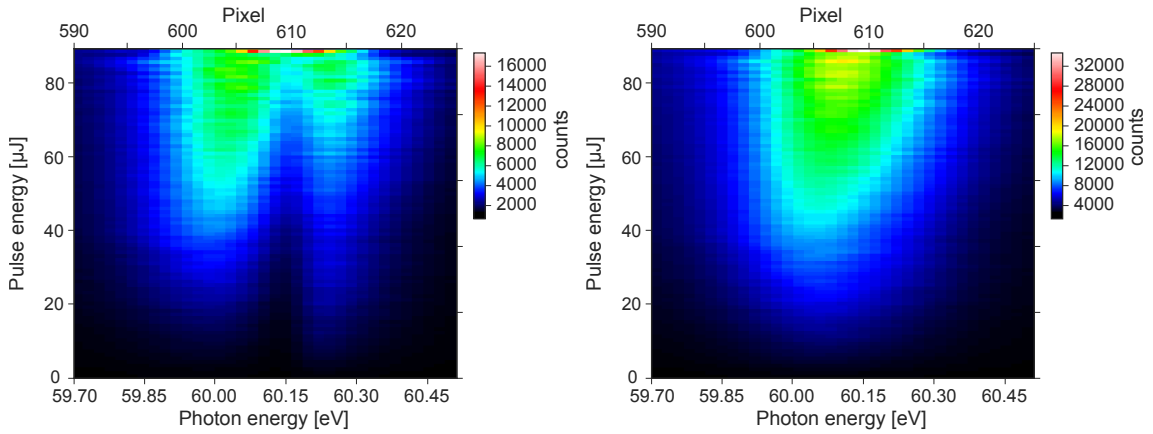

Figure 3.6: Sorted spectra of intensity scan for the spectrometer, Pixis (left) and the reference spectrometer, PCO, already resampled (right)

The spectra of the reference spectrometer were averaged accordingly for every histogram step. Next, the resampling was performed with the respective parameters calculated in Ch.3.1. The quality of the resampling can be seen in Fig.A.7. Finally the optical density (eq. 3.1) was computed. The result is depicted in Fig. 3.7.

The optical density shows a Fano profile for low intensities, which evolves into a Lorentzian for higher intensities. This gets even clearer when a lineout is plotted, Fig. 3.8. Before turning to the analysis of the Fano-Lorentz-transformation, a few things about the plot itself shall be noted.
The plot looks a little grainy. Although averaged over several dozens of spectra, this is still due to the very fluctuating spectra generated by the FEL. As described above an average should contain at least 80 spectra. In Fig. A.3 can be verified that at least 100 spectra are averaged for the different histogram steps up to 85µJ. It can also be seen that the average is not constant but varies a lot.
It should be noted as well that Fig. 3.7 only contains the energy range 59.7−60.5 eV, corresponding to pixel 590-625, as only this interval was relevant to the FEL spectrum. The full OD from the acquired spectra is depicted in Fig.A.8-A.10 Structures beyond this interval descend form imperfections in the resampling process or mechanisms described above, which cannot be corrected by this process. This leads to a deviation of the spectra resulting never the less in structures in the OD where no physical effect occurred in the target.
The energy calibration which was used above will be calculated in the next part

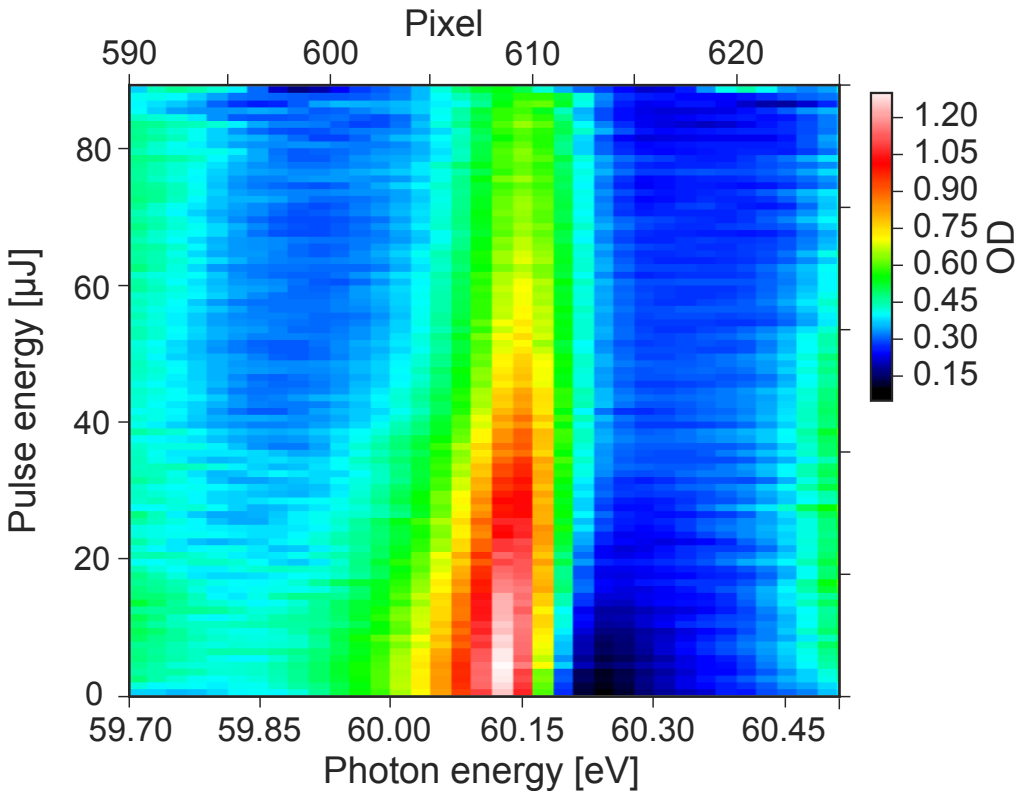

Figure 3.7: Optical density for the helium intensity scan centered and zoomed in at the 2s2p doubly excited state at 60.15 eV for pulse energies of $0 - 90\mu J$

from fitting parameters of the Fano line shape and the corresponding theory values. This path had to be chosen since the reference spectrometer is not permanently calibrated and has to be gauged with an offline spectrometer after every alignment in the beam distribution. This calibration was not conducted in the first shift.

3.4 Fano-fits

To quantify the results of the measurement the optical density was fitted with a Fano lineshape Eq. (1.36) from Ch.1.3.1.

3.4.1 fitting process

The fit was limited to the interval pixel 600 to 620. This served to circumvent the wings described above and is legitimized since the Fano profile is fully enclosed by this interval. The spectrometer in the setup exhibits a limited

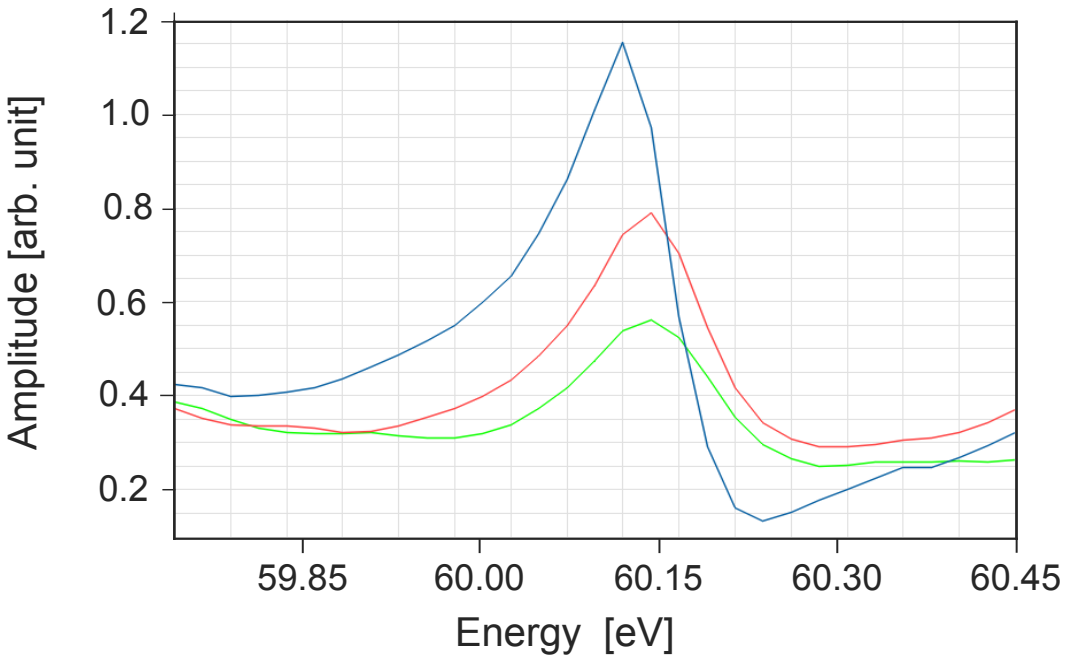

Figure 3.8: Lineouts of the optical densities in Fig.3.7 for pulse energies of $3\mu J$ (blue), $40\mu J$ (red), $80\mu J$ (green).

resolution. A point-like source is therefore imaged to an Airy function rather than a delta function. In this setup this originates form the fact that an entrance slit (2D-Slit) was used, Ch. 2.3. Also small misalignment of the grating can impact the resolution. To account for this broadening, the fitting algorithm convolutes the Fano line shape with such a function before evaluating the deviation to the dataset. However, the Airy function makes things complicated which is why it is approximated by a Gaussian. The parameter of the width represents the resolution and can either be an additional subject to the fitting algorithm if unknown or once obtained enter as a fixed quantity. The area under the Gaussian is one. Thereby a convolution with this function does not impact the total area under the function to be fitted but only the shape. In other words it changes the spectral intensity distribution but not the total intesnsity. In the case of an asymmetric line shape, like the Fano profile, this generates a more symmetric function.

3.4.2 energy calibration

In the first step the resonance energy E_{Res}, the spectral width Γ and the spectral resolution are retrieved from the fit. Therefore the q-parameter is

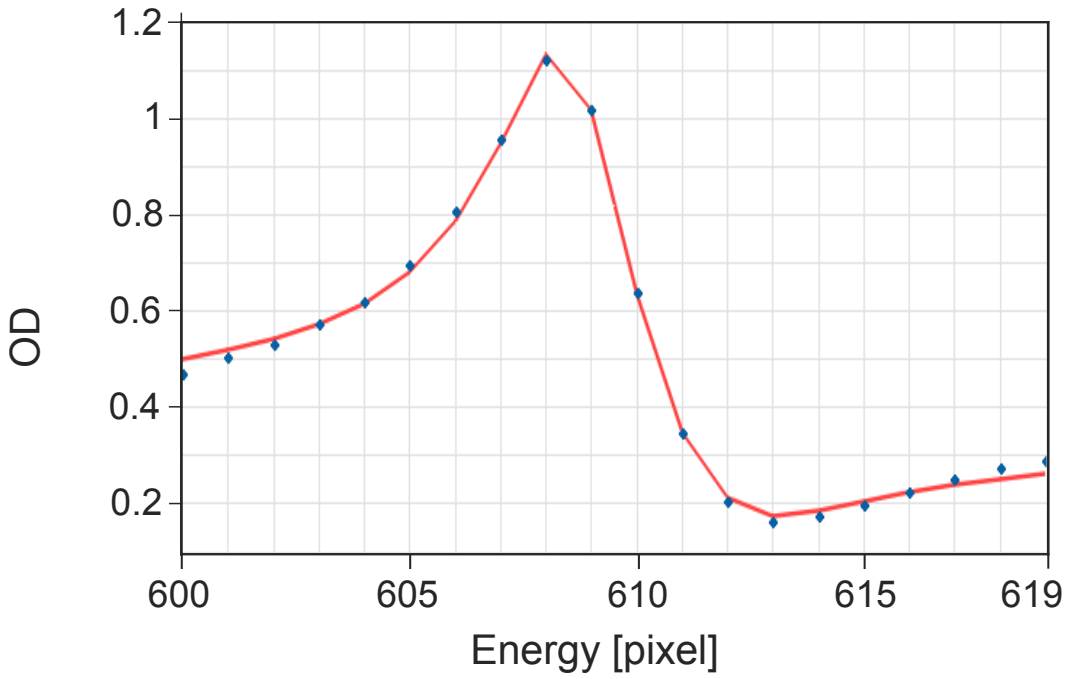

Figure 3.9: Lineouts of the optical densities in Fig.3.7 for $7\mu J$ pulse energy (blue), and the fitted Fano line shape(red).

fixed to its literature value of -2.7 while the fitting algorithm is performed for the first 5 histogram steps, corresponding to the 0 - 4 μJ. The quality of this fitting is presented in Fig.3.9 Since the q-parameter is unit less, it is independent of the energy calibration and can be used as the starting point. The resulting fitting parameters in units of pixel can be then connected with the literature values in meV, presented in table 3.1.

	fit-parameter	literature
E_{Res}	609.50 px	60,15 eV
Γ	1.60 px	37 meV
spectrometer resolution	2.85 px	

Table 3.1: Parameter of the Fano-fit for low energies set in connection to the literature values for the low intensity regime. Values from [10].

The literature values can be assumed here since we are in the perturbative regime at these low intensities. With these values the energy calibration can be executed. The resonance is at 60.15eV corresponding to pixel 609.5, with the pixel size of 23.15 meV. Furthermore the spectrometer resolution can be read. It computes to 2.85 pixel which corresponds to 65.9 meV.

From previous HHG experiments a resolution of 47 meV is known. Since the 2D-entrance slit to the spectrometer is used and no longer be presented by the focus in the target-volume, this deviation appears plausible. Also the resolution of the reference spectrometer can have a negative impact. However this was neglected due the high complexity evaluating the different resolutions before determining the OD. The resolution is also depended on the quality of the alignment, which was performed with great care, but never the less can exhibit smallest misalignment.

3.4.3 fitting fano parameters

With the energy calibration and the resolution (66 meV) now fixed, a trace of the q-parameter can be computed. Hence the fitting algorithm was repeated, this time for all the histogram steps and with fixed resolution. The values for low energy regime from literature were entered as guess values for the resonance energy, the width and the q-parameter.
The traces for the q-parameter is depicted in Fig. 3.10.

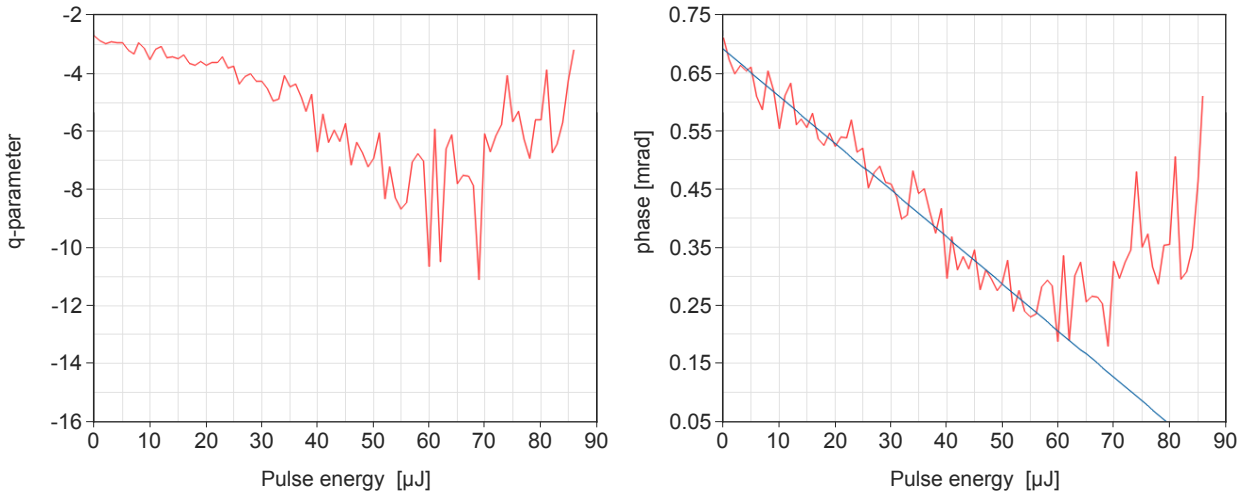

Figure 3.10: Trace of the q-parameter (left) and the corresponding phase (right) fitted with a linear function (blue)

The q-parameter is related by Eq.(1.41) to the phase between the two channels of auto ionization and direct ionization. It is much easier to be interpreted since it obeys a linear relation to changes in the energy levels. It is depicted in Fig.3.10
Up to 60μJ a negative linear trend can be identified. This is supported by the

linear fit (up to $57\mu J$). The behavior indicates a transformation to a more symmetric lane shape, from Fano, close to 1.5mrad, to Lorentzian, close to zero mrad. This is in accordance with the lineouts of the OD in Fig. 3.9 .
The line shape changes occur due to strong field coupling on ultra short timescales. The pulse shifts the energy level, which leads to the accumulation of phase.
The same effect has been found with non-resonant ponderomotive coupling [2]. In our case the dressing happens resonantly.
The result coincides also with simulations considering the coupling between a ground state and the double exited state and a continuum, [16].
The resonance energy Fig.3.11 in this interval shows a linear behavior. It shifts slightly to smaller photon energies by 4.6 meV.

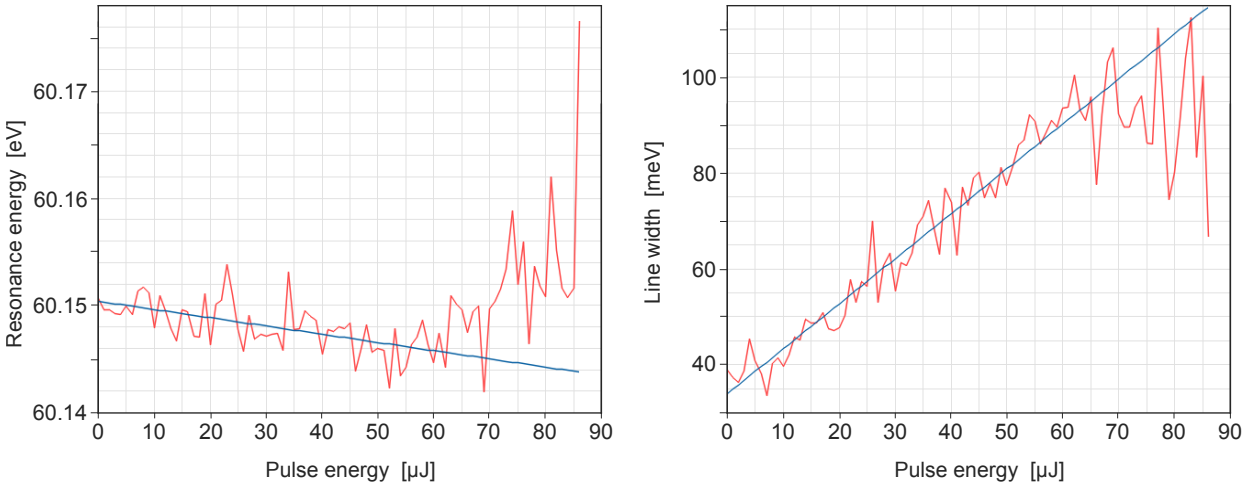

Figure 3.11: Trace (red) of the resonance energy E_{res}(left) and of the line width Γ (right) to the fitted Fano line shape. The fitting parameters were fitted with a linear function up to pulse energies of 60 μJ to underline the linear behavior.

The FLASH pulse duration was estimated at a neon experiment to 50 fs. With the focus size of $20\mu m$ and a pulse enegery of $100\mu J$ the intensity can be estimated to 10^{14} W/cm^2. Since the life time of the 2s2p state in helium of 17fs is significantly shorter than the pulse duration, a strong shift of the resonance energy is expected. The value can be estimated by

$$\bar{\Omega}_{nm} = \frac{1}{2} E_1(t) D_{nm} (1 - \frac{i}{q_r}) \qquad \text{(from [17])} \qquad (3.2)$$

with the envelop of the electric field ($E_1 \approx 0.1$ a.u. at this intensity) and the dipole element ($D_{nm} \approx 0.035$ a.u.), yielding an expected shift of about 27meV. The shift is larger than the observed 4.6 meV. This indicates a coherence time of the FLASH pulse much shorter than the 17 fs of the state.
The interaction can therefore be considered to be in the impulsive regime. The phase kick leads to a change in the quantum interferometer and by the direct mapping to the change of the q-factor and hence line shape.
This allows for time resolved measurements much higher than the 50fs length of the pulse. It is manifested when the coherence time is estimated from the bandwidth of the FLASH.

Beyond a pulse energy of 60 μJ the resonance energy and the phase saturate and exhibits strong noise. Similar behavior can be observed from the line width Γ, Fig. 3.11.

This can originate from different technicalities. One possibility would be saturation in the GMDs and therefore incorrect recording of the pulse energy, which has a direct influence on the result via the histogram process. It is crosschecked with a correlation of the binned spectra in the histogram of the Pixis spectrometer and the according GMD values. As can be seen in Fig.A.2, the correlation exists also for photon energies $> 60\mu$J and the GMDs can therefore be assumed to operate correctly.
Another reasons can be found in terminal effects at the optical components. Higher intensities can lead to tension in the substrate of the ellipsoidal or distribution mirrors. This can for example change the curvature of the mirror and hence a longitudinal shift of the focus. Although the pulses exhibit increasing energies, it is compensated by the (proportional) distortion, leading to conditions in the target which are equivalent to saturation. Also a local change in the surfaces of the optical components can influence the reflected wavefront and manipulate the focus.
A third possibility is the interaction with the gas of the absorber. For high intensities, the gas absorber is almost empty. In order to lower the pulse energy it is filled with a noble gas. When the gas density reaches a certain regime, propagation effects have to be considered. They can lead to a systematic change in the temporal structure of the pulse, e.g. a chirp. For the

given SASE pulses this could be required to observe the clear trend below 60μJ.

In a more physical approach to explain this noisy behavior the complex interplay of the multiple time scales can be considered. The quantities involved in this system are the life time of the doubly excited state, the pulse structure of the SASE and the Rabi frequency induced by the strong field coupling. When any of these features are in resonance, new effects can occur. Also the appearance of strong non-linear effect can be considered. Since the spectra are accumulated such effects could even be embedded in the shift of the resonance energy, disguising themselves as a dressing of the system.

4 Conclusion

One objective of this work was to accomplish experiments with halogenated hydrocarbon molecules and noble gases at FLASH. For this purpose a novel beam line was extended and essential components developed and redesigned to achieve this goal. The challenges of high intensities, polymerizing halogenated hydro carbonate and time critical beam time were faced and met with accelerated and automatized systems (stage system, walk-off correction), easier accessible and quick to assemble components (cell, filter unit) and devices providing high flexibility by offering more than one setting (spectrometer grating and filter unit). All these components have been successfully implemented and commissioned. This ground work can thus be considered as a basis for future measurement campaigns at FEL facilities. The accomplishments of this marks a major milestone of this work.

A further subject to this thesis was the investigation of the doubly excited state 2s2p in helium. While the line shape modification has been investigated before with intense VIS field [2], the goal of this experiment has been to examine this modification with strong and resonant XUV pulses. The coupling of the autoionizing state with a strong XUV field allowed to investigate electron-electron correlation effects and gave a glimpse of the temporal characteristics of the FLASH.

The results showed besides the expected behavior of a linear phase with increasing intensity, some new phenomena whose origin could not be identified yet. For example the small shift of the resonance energy gives rise to the question whether this shift originates from a slightly smaller coherence time compared to the lifetime of the doubly excited state (17fs) or other temporal structure on this scale, or if other effects are covered underneath which exhibit a correlation to a quantity which is washed out by the accumulation of several hundred spectra.

Further investigation is also required to understand the abrupt change in the

behavior for most of the Fano parameters at pulse energies beyond 60μJ. Here, explanations of technical nature, hardware and software, have been provided. Yet more intriguing would be if this behavior could be related to a more fundamental process, where the complex interplay of several time quantities, like the lifetime of the doubly excited state, the pulse structure of the SASE and the strong-field coupling with its quantity the Rabi frequency has been discussed.
To clarify this and other open questions, it would be interesting to conduct further analysis on the obtained data, correlating with a variety of parameters such as the spectral distribution which could be connected to certain temporal structures or the spectral blue or red detuning, which could give more insight on line shape transformation for dressed states.

Though the helium atom is clearly the most simple system providing two electrons and very well described by theory, many phenomena are not yet understood. It therefore presents the ideal playground for further investigation in electron correlation.

Bibliography

[1] Ugo Fano. Effects of configuration interaction on intensities and phase shifts. *Physical Review*, 124(6), December 1962.

[2] Christian Ott, Andreas Kaldun, Philipp Raith, Kristina Meyer, Martin Laux, Jörg Evers, Christoph H. Keitel, Chris H. Greene, and Thomas Pfeifer. Lorentz meets fano in spectral line shapes: A universal phase and its laser control. *Science*, 340:716–720, May 2013.

[3] R. W. Boyd. *Nonlinear Optics*. Academic Press, 2. edition, 2003.

[4] C. Rullière. *Femtosecond Laser Pulses: Principles and Experiments*. Springer, New York, 2005.

[5] Christian Ott, Andreas Kaldun, Luca Argenti, Philipp Raith, Kristina Meyer, Martin Laux, Yizhu Zhang, Alexander Blättermann, Steffen Hagstotz, Thomas Ding, Robert Heck, Javier Madroñero, Fernando Martín, and Thomas Pfeifer. Reconstruction and control of a time-dependent two-electron wave packet. *Nature*, 516:374–378, December 2014.

[6] Christian Ott. *Attosecond multidimensional interferometry of single and two correlated electrons in atoms*. PhD thesis, Ruperto-Carola-University of Heidelberg, July 2012.

[7] P. Lambropoulos and P. Zoller. Autoionizing states in strong laser fields. *Physical Review A*, 24(1), July 1981.

[8] Alexander Blättermann, Christian Ott, Andreas Kaldun, Thomas Ding, and Thomas Pfeifer. Two-dimensional spectral interpretation of time-dependent absorption near laser-coupled resonances. *Journal of Physics B: Atomic, Molecular and Optical Physics*, 47, June 2014.

[9] F. Prats J. W. Cooper, U. Fano. Classification of two-electron excitation levels of helium. *Phys. Rev. Lett.*, 10, 1963.

[10] M. Domke J. D. Bozek P. A. Heimann A. S. Schlachter K. Schulz, G. Kaindl and J. M. Rost. Observation of new rydberg series and resonances in doubly excited helium at ultrahigh resolution. *Phys. Rev. Lett.*, 77, 1996.

[11] G. Remmers G. Kaindl M. Domke, K. Schulz and D. Wintgen. High-resolution study of 1po double-excitation states in helium. *Phys. Rev. A*, 53, 1996.

[12] Kwang-Je Kim Zhirong Huang. Review of x-ray free-electron laser theory. *Physical Review Special Topics*, 10, (2007).

[13] M. Kuhlmann E. Ploenjes T. Noll F. Siewert R. Treusch K. Tiedtke R. Reininger M.D. Roper M.A. Bowler F.M. Quinn G. Brenner, S. Kapitzki and J. Feldhaus. First results from the online variable line spacing grating spectrometer at flash. *Nuclear Instruments and Methods in Physics Research A*, 635, 2011.

[14] N. von Bargen L. Bittner S. Bonfigt S. Düsterer B. Faatz U. Frühling M. Gensch Ch. Gerth N. Guerassimova U. Hahn T. Hans M. Hesse K. Honkavaar U. Jastrow P. Juranic S. Kapitzki B. Keitel T. Kracht M. Kuhlmann W. B. Li M. Martins T Nuñez E. Plönjes H. Redlin E. L. Saldin E. A. Schneidmiller J. R. Schneider S. Schreiber N. Stojanovic F. Tavella S. Toleikis R. Treusch H. Weigelt M. Wellhöfer H. Wabnitz M. V. Yurkov K. Tiedtke, A Azima and J Feldhaus. The soft x-ray free-electron laser flash at desy: beamlines, diagnostics and end-stations. *New J. Phys.*, 11, 2009.

[15] Marc Rebholz. Design and construction of an experimental setup for multidimensional spectroscopy in the xuv/ soft-x-ray spectral region. Master's thesis, Ruperto-Carola-University of Heidelberg, 2015.

[16] A. Magunia. Elektronen-korrelation in helium unter einfluss intensiver xuv-laserpulse. Master's thesis, Ruperto-Carola-University of Heidelberg, 2016.

[17] Lambropoulos Themelis and Meyer. Ionization dynamics in double resonance involving autoionizing states in helium: the effect of pulse shapes. *J. Phys. B: At. Mol. Opt. Phys.*, 37, October 2004.

Appendix

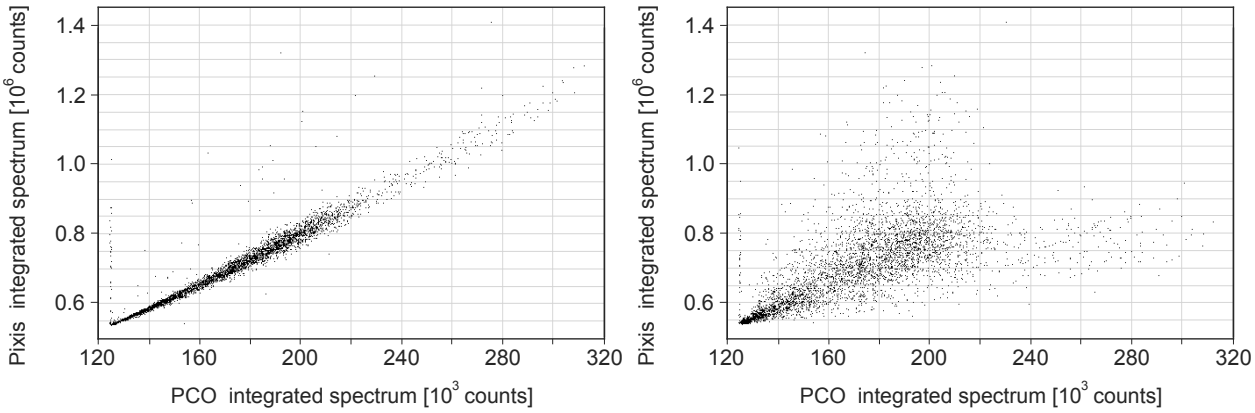

Figure .1: Correlation of the integrated spectra from the PCO and the Pixis. This serves to proof the viability of the BunchID concept. **left:** BunchID synchronized, **right:** BunchID relation shifted by +1.

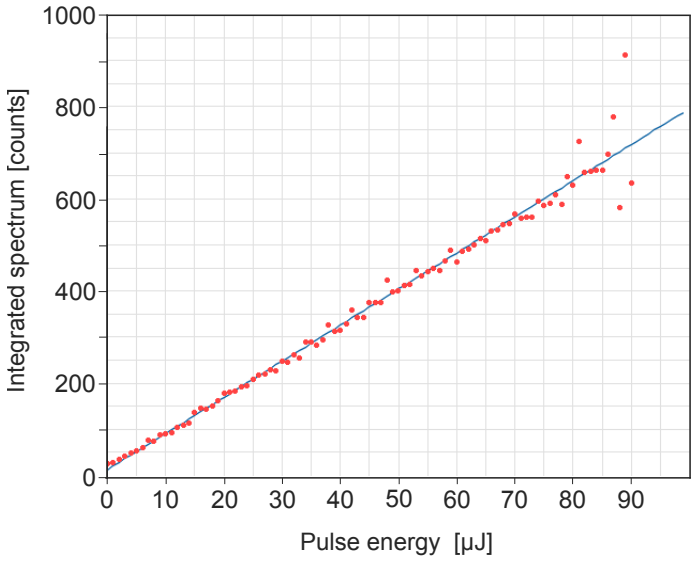

Figure .2: Integrated spectra of the Pixis over the pulse energy measured with the GMD (post absorber) during the intensity scan. It does proof that the GMD operates correctly.

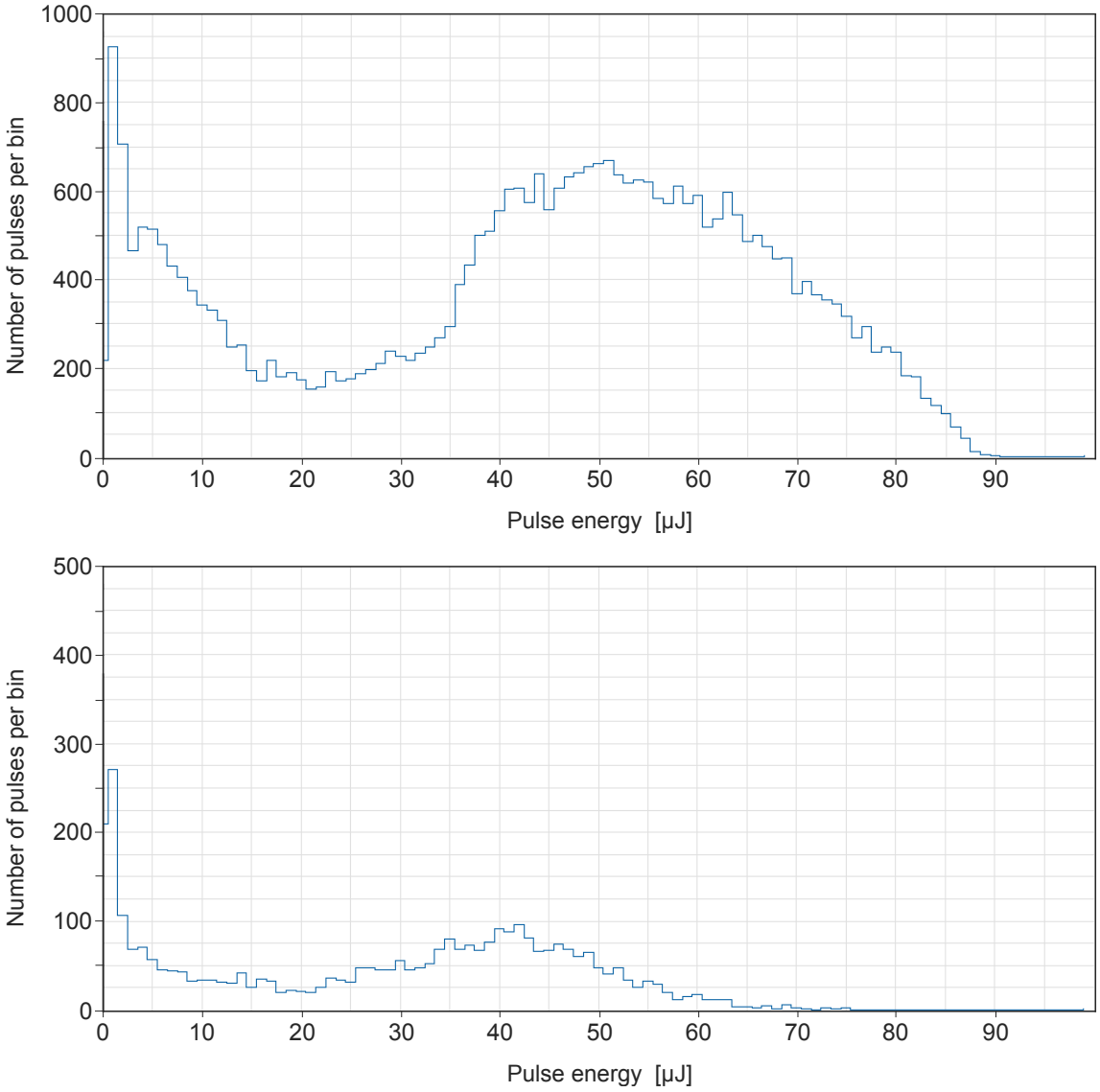

Figure .3: Histogram of the BunchIDs over the the pulse energy (post absorber). **top:** for the intensity scan with helium, **bottom:** for the reference intensity scan. The dip in the middle originates from the fact that the absorber was driven to perform the measurement. The reference measurement was conducted with much lower statistic

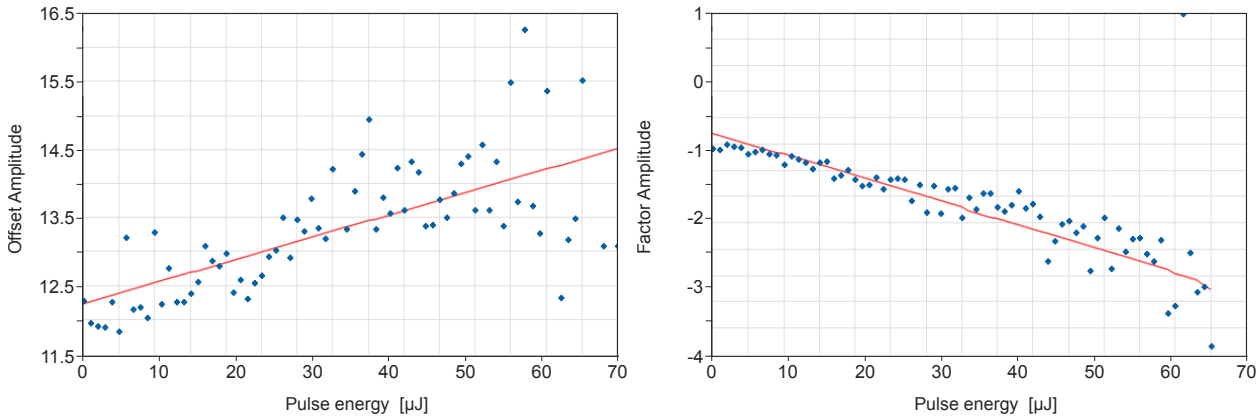

Figure .4: Resampling parameter for the amplitude, offset (left) and factor (right), over the (pulse energy post absorber). The data points are linearly fitted (red).

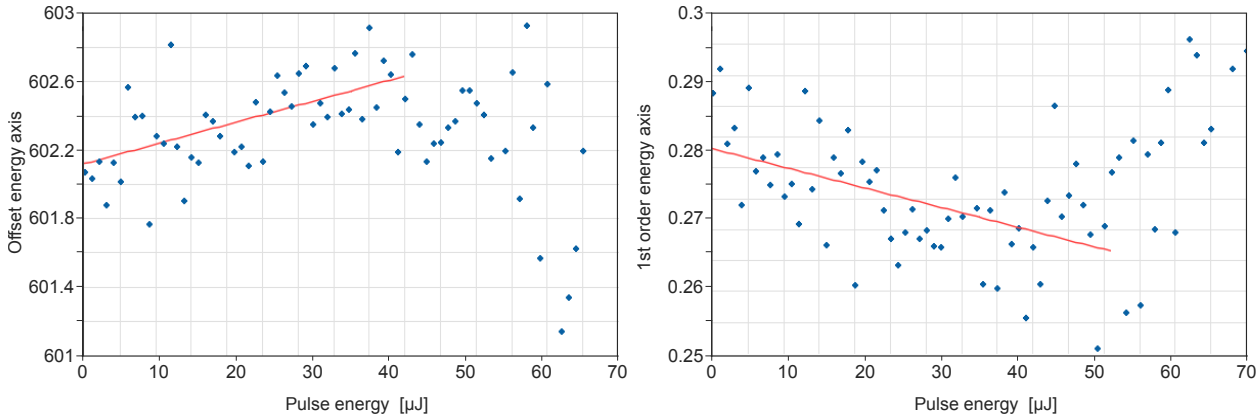

Figure .5: Resampling parameter for the energy axis [in pixel], offset (left) and 1st order (right), over the (pulse energy post absorber). The data points are linearly fitted (red) for the interval up to 45μJ and extrapolated thereafter for the resampling process.

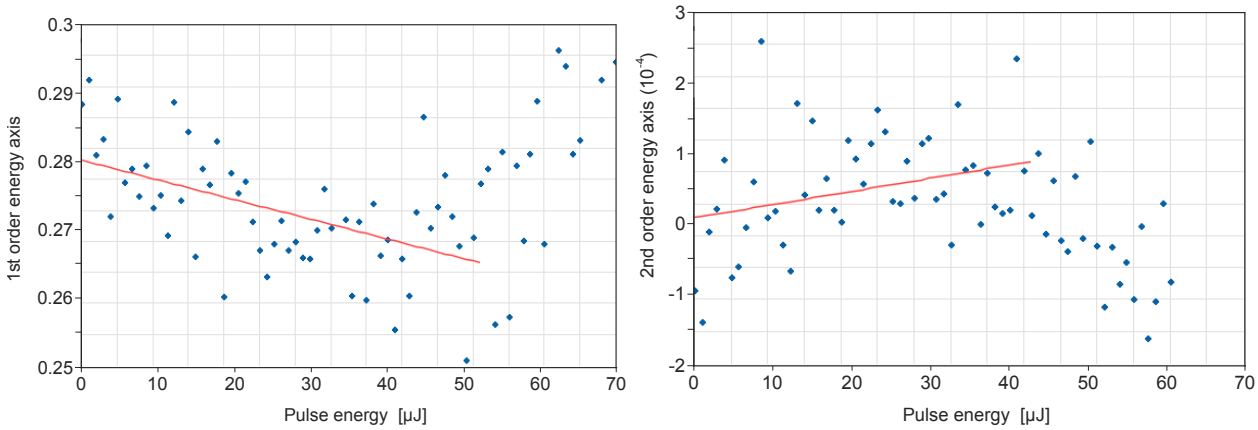

Figure .6: Resampling parameter for the energy axis [in pixel], 2nd (left) and 3rd order (right), over the (pulse energy post absorber). The data points are linearly fitted (red) for the interval up to 45μJ and extrapolated thereafter for the resampling process. As the values are in the 10−4 and 10−6 regime respectively, the resampling can be assumed linear.

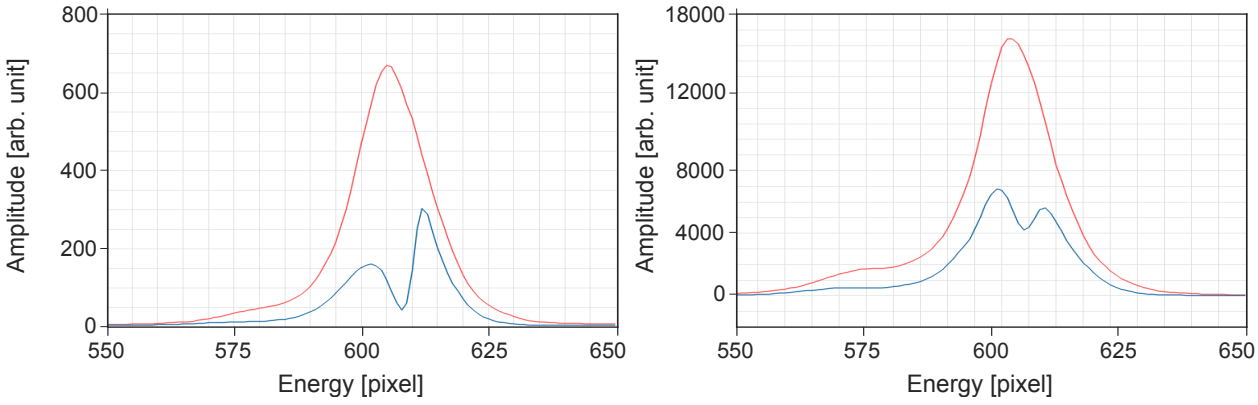

Figure .7: Lineout of the absorption spectrum (blue) and the reference spectrum (red) at 3μJ (left) and 80 μJ (right).

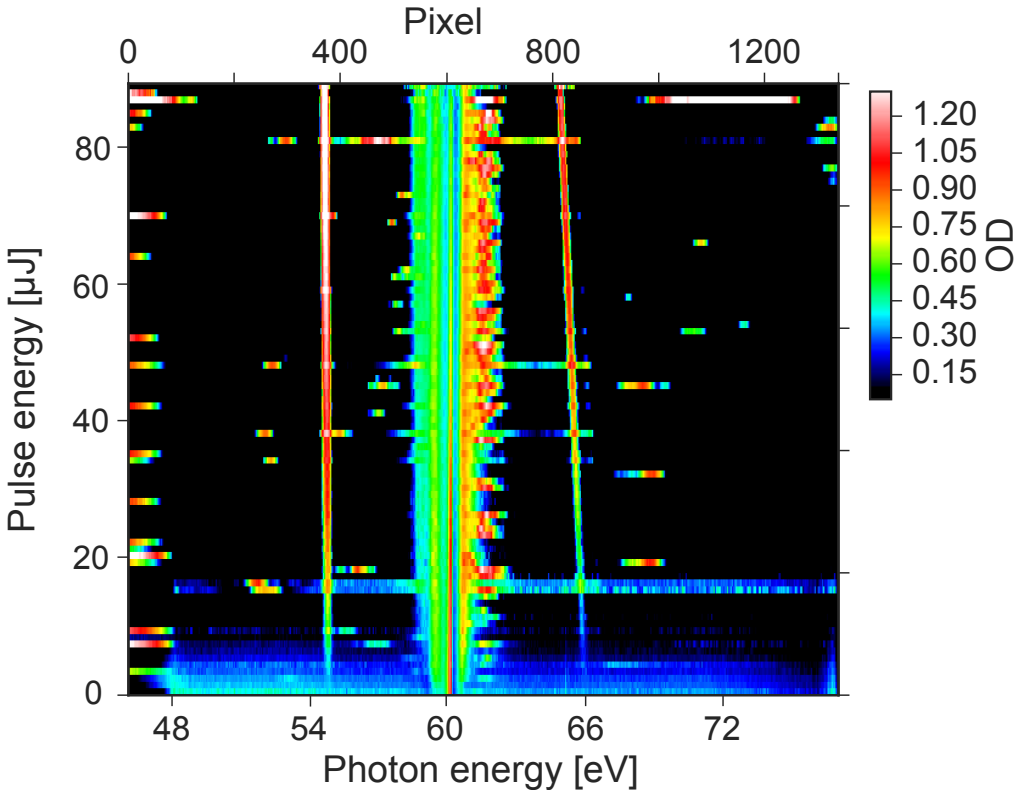

Figure .8: Optical density for the full detector chip over the pulse energy (post absorber).

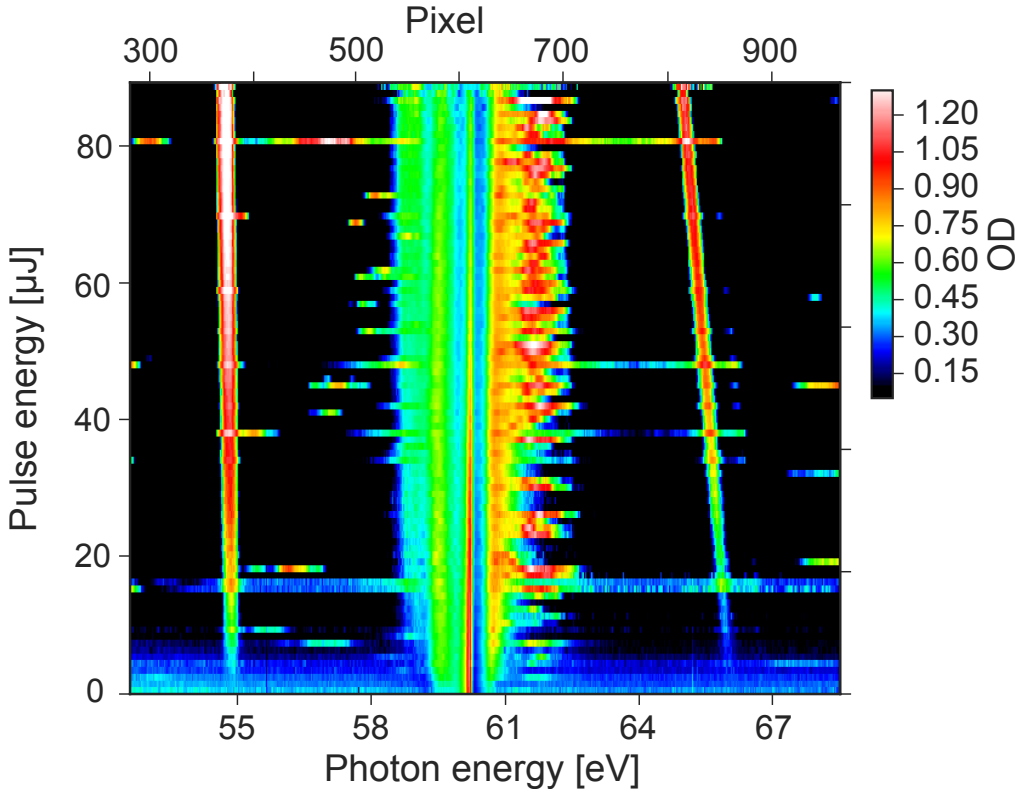

Figure .9: Optical density over the pulse energy (post absorber), zoomed in to pixel 280-980 for better presentation of the side-band structures. They originate from a shift in the offset of the PCO on the edges of its detector chip. The resulting deviation was not compensated during the resampling and led to this structure.

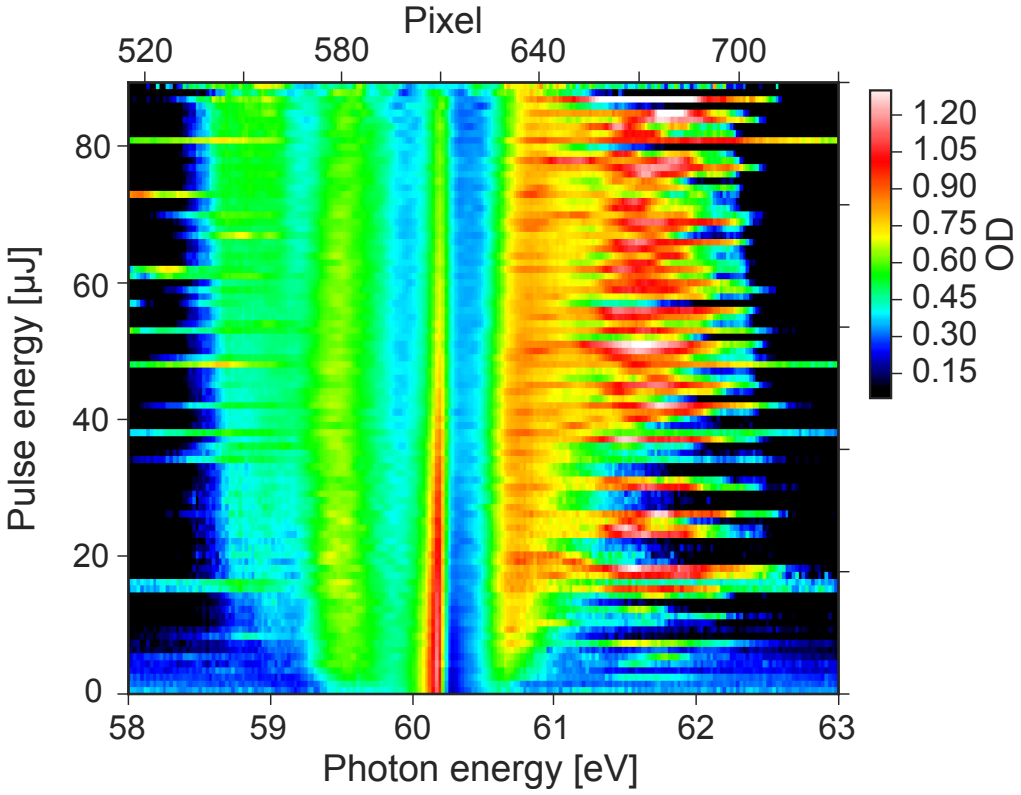

Figure .10: Optical density over the pulse energy (post absorber), zoomed in to pixel 520-730 for better presentation of the side wings. They originate from a imperfect resampling process and other reasons, see Ch. 3.2. The deviation of both spectra, though no physical effect in the target was involved, lead to this structure.

Acknowledgement

An dieser Stelle möchte mich herzlich bei allen Mitarbeitern der Abteilung Pfeifer am Max-Planck-Institut für Kernphysik für die angenehme Arbeitsatmosphäre und das lehrreiche vergangene Jahr bedanken.

Mein besonderer Dank gilt:

Prof. Dr. Thomas Pfeifer für die Ermöglichung meiner Masterarbeit in seiner Arbeitsgruppe, sowie seine ununterbrochene Motivation und Wertschätzung für die geleistete Arbeit.
Priv. Doz. Dr. Robert Moshammer für die Übernahme des Zweitgutachtens meiner Arbeit und seine Beratung während der Vorbereitung auf die Strahlzeit-Kampagne.

Dr. Christian Ott für die zahlreichen physikalischen Erläuterungen und Denkanstöße, die enorme Unterstützung während der Zeit in Hamburg, sowie davor aus großer Distanz und danach bei der Verarbeitung der Messergebnisse.

Dem Kernteam des Experiments:
Thomas Ding, **Marc Rebholz** und **Maximilian Hartmann** für die großartige Zusammenarbeit bei der Planung und dem Aufbau des Experiments über das gesamte Jahr hinweg. Für die langen gemeinsamen Stunden während der Vorbereitung im Labor in Heidelberg und in der Experimentierhalle am FLASH und die schlaflosen Nächte während der Kampagne. Weiterhin auch für das umfangreiche Feedback bei Verfassung und Korrektur dieser Arbeit.

Dr. Kristina Meyer für die Mitarbeit im Labor und die fachlichen Anregungen.
Veit Stoos für seine Unterstützung durch Arbeit und Wartung am Laser, insbesondere in der heißen Test-Phase vor der Kampagne.
Dr. Alexander Blättermann, Paul Birk und Martin Laux für das kollegiale Miteinander im Labor und die zahlreichen hilfreichen Tipps.

Alexander Magunia und David Wachs für die Unterstützung während und um die Strahlzeit-Kampagne herum, insbesondere für die Erstjustage des experimentellen Aufbaus an der Endstation.

Dr. Claus Dieter Schröter für seine Beratung bei der Umsetzung des Experiments.
Bernd Knape für die tatkräftige Unterstützung in allen technischen Aspekten rund um das Experiment.
Christian Kaiser für den fachmännischen Aufbau des Setups an der Endstation.

Weiterhin **Erland Müller** vom DESY für seine zuvorkommende und herausragende technische Unterstützung bei der IT-Infrastruktur und Datenverarbeitung am FLASH.

Zuletzt gilt mein großer Dank meinem persönlichen Umfeld,
I. Weigl, **Prof. HG.** und **Dr. C. Penzel**, und meiner Familie, vor allem meinen Eltern **Dr. P.** und **Dr. G. Aufleger**, die mich ununterbrochen unterstützen und begleiten und dadurch erst meine persönliche und professionelle Entwicklung ermöglicht haben.

Erklärung:

Ich versichere hiermit, dass ich diese Arbeit selbstständig verfasst, und keine anderen als die angegebenen Quellen und Hilfsmittel benutzt habe.

Heidelberg, den 14. Oktober 2016 .....

Declaration of authorship:

I hereby declare that this thesis I am submitting is entirely my own original work except where indicated other wise.

Heidelberg, October 14th 2016 .....